Finite-volume analysis of a hybrid nanofluid flow in a tilted porous square cavity under multi-segment heating and magnetic field

A Thesis Submitted in Partial Fulfillment of The Requirements for Awarding the Degree Of

Master of Automobile Engineering
Faculty of Engineering and Technology

Submitted by

SOBHAN PANDIT

Registration No.- **140887 of 2017-18**

Examination Roll No.- **M4AUT23003**

Under the guidance of

Prof.(Dr.) Dipankar Sanyal
Dr Milan Kumar Mondal

DEPARTMENT OF MECHANICAL ENGINEERING
JADAVPUR UNIVERSITY
KOLKATA -700032
INDIA

2023

FACULTY OF ENGINEERING AND TECHNOLOGY

DEPARTMENT OF MECHANICAL ENGINEERING

JADAVPUR UNIVERSITY

KOLKATA

DECLARATION OF ORIGINALITY

AND

COMPLIANCE OF ACADEMIC ETHICS

*I hereby declare that this thesis contains a literature survey and original research work by the undersigned candidate as part of his **Master of Engineering** studies.*

All information in this document has been obtained and presented in accordance with academic rules and ethical conduct.

I also declare that, as required by these rules and conduct, I have fully cited and referenced all materials and results that are not original to this work.

Name : **Sobhan Pandit**

Examination Roll No : **M4AUT23003**

Thesis Title : Finite-volume analysis of a hybrid nanofluid flow in a tilted porous square cavity under multi-segment heating and magnetic field.

Signature :

Date :

FACULTY OF ENGINEERING AND TECHNOLOGY

DEPARTMENT OF MECHANICAL ENGINEERING

JADAVPUR UNIVERSITY

KOLKATA

CERTIFICATE OF RECOMMENDATION

We hereby recommend that this thesis under our supervision by **Sobhan Pandit**, entitled, **"Finite-volume analysis of a hybrid nanofluid flow in a tilted porous square cavity under multi-segment heating and magnetic field"** be accepted in partial fulfilment for awarding the degree of Master of Automobile Engineering under Department of Mechanical Engineering of Jadavpur University.

_____

Dr. Milan Kumar Mondal
Thesis Advisor
Dept. of Mechanical Engineering
Medinipur Sadar Govt. Polytechnic
Technical Education and Training,
Govt. of West Bengal

_____

Prof. (Dr.) Dipankar Sanyal
Thesis Advisor
Dept. of Mechanical Engineering
Jadavpur University,Kolkata

_____

Prof. (Dr.) Amit Karmakar
Head of the Department
Dept. of Mechanical Engineering
Jadavpur University,Kolkata

_____

Prof. (Dr.) Ardhendu Ghoshal
DEAN
Faculty of Engineering & Technology
Jadavpur University,Kolkata

FACULTY OF ENGINEERING AND TECHNOLOGY

DEPARTMENT OF MECHANICAL ENGINEERING

JADAVPUR UNIVERSITY

KOLKATA

CERTIFICATE OF APPROVAL

The foregoing thesis entitled "**Finite-volume analysis of a hybrid nanofluid flow in a tilted porous square cavity under multi-segment heating and magnetic field"** is hereby approved as a creditable study of an engineering subject carried out and presented in a manner satisfactory to warrant its acceptance as a prerequisite to the degree for which it has been submitted. It is notified to be understood that by this approval, the undersigned do not necessarily endorse or approve any statement made, opinion expressed and conclusion drawn therein but approve the thesis only for the purpose for which it has been submitted.

Committee of final examination for evaluation of thesis;

…… …….

…… …….

……. ……...

Signature of Examiners

Acknowledgements

Jadavpur University has provided me an incredible learning since last couple of years. It has prolonged me academically and personally. To finish this entire task of writing thesis was never painless for me and it would have not been completed without noble contribution of the people around me. The extensive association with the respected teachers and friends in the Neptune lab, Department of Mechanical Engineering was the most quality time of my academic career and I have got adequate inspiration for breathing in the prospect of future. The dedication, devotions, sincerity, caring I found in all the teachers for the scholars, I will probably never find elsewhere. I am very grateful to the people that have been with me to share this whole experience.

I cannot start without acknowledging Prof. Dipankar Sanyal for providing useful suggestions and assistance extended regarding present problem and encouraged me to carry the things in the right direction. Likewise, I am undoubtedly indebted to mention the unparalleled contribution of Dr. Milan Kumar Mondal, the friend, philosopher, guide and my inspiration whose persistent advice, guidance, timeless and tireless assistance, and above all his enthusiastic indulgence accelerated me to this venture the fruition of which is the present study.

I appreciate all that I have learned from them as an advisor, teacher, mentor and especially as friend. There cannot be any match to describe the role they played to complete this thesis. They took the pain of introducing the basic subjects, use of computational methods, writing research papers and everything about research. I am inspired with their dedication during the moment I have spent with them. They had spared their precious time on my every need during the whole work of my thesis. Their simplified method of describing problems, conducting experiments and presenting them in an easy and nice way will always be my pathfinder during my academic career. Finally, I thank my parents for their constant support, encouragement and words of confidence.

Dept. of Mechanical Engineering
Jadavpur University, Kolkata, India

_____
[SOBHAN PANDIT]

ABSTRACT

An interesting case of segmented heating in a tilted porous square cavity packed with hybrid $Cu-Al_2O_3$/water nanofluid with segmented magneto-hydrodynamic (MHD) has been studied for its widespread applications in medical electronics and health industries. The results are generated by using finite volume technique based on SIMPLE algorithm solved by TDMA developed in-house for the coupled transportation equations and appropriate boundary conditions. Effects of geometric variations and hybrid nanofluid volume concentration along with the parameters, namely Darcy-Rayleigh number, Darcy number, Hartmann number, magnetic field strength and angle under different combinations of segmented heating and magnetization. More stress has been laid on the physical understanding of the results. Further investigation is necessary for arriving at the optimized arrangement for achieving the control of the zone with the maximum heating.

LIST OF TABLES

LIST OF FIGURES

NOMENCLATURE

AR	Aspect Ratio		***Greek symbols***
B	Magnetic induced fields (Tesla, N A^{-1} m^{-2})	α	thermal diffusivity (m^2 s^{-1})
Da	Darcy Number	ζ	thermal expansion coefficient (K^{-1})
g	Gravitational acceleration (m s^{-2})	β	inclination angle of the magnetic field (degree)
H	Cavity height /length scale (m)	γ	Cavity angle (degree)
Ha	Hartmann number	ε	Porosity index
K	Porous medium permeability (m^2)	θ	Non dimensional temperature
Nu	average Nusselt number	λ_B	magnetic fields parameter
P	Unit less pressure	μ	absolute viscosity
Pr	Prandtl number	ν	kinematic viscosity (m^2 s^{-1})
Ra	fluid Rayleigh number	ρ	density (kg m^{-3})
Ra_m	Darcy–Rayleigh number	τ	unit less time
		φ	hybrid nano scale particles volume fraction
T	time (s)	ψ	dimensionless stream function
T	temperature (K)	Π	dimensionless heat function
u, v	velocity components (m s^{-1})		***Subscripts***
U, V	Unit less velocity components	a	ambient
x, y	Cartesian coordinates (m)	c	cold
X, Y	unit less coordinates	f	base fluid
w_b	width of active magnetic fields (m)	h	hot
		max	maximum
		s	solid

CONTENTS

CHAPTER 1: INTRODUCTION

Overview

A little word ‘nano’ has progressed from the world of future to the world of present. Nanotechnology is making its marks in industries for some decades and a lot of applications are already standardized. Nano scaled materials have unique physical, chemical and mechanical properties that could be tailored for an extensive variety of applications resembling next-generation computer chips, aerospace components and pollutant eliminating additives. Nanoparticles are derived from carbon nanotubes, metals and their oxides and carbides. Nanofluids are engineered colloidal suspensions of nanoparticles in a base fluid like ethylene glycol, water and oil.

Elevated thermal conductivity of some nanoparticles than the hoist fluid and high ratio of surface area to volume fraction of the particles hold promise for a class of nanofluids to be more effective in designing compact heat exchangers. These are expected to bring in further compactness that the prevalent use of extended surfaces along with fluid suction and injection fails to provide. High area-to-volume ratios of the particles are also suitable as fuel additives for the absorption of pollutants. Ultimately, the development of nanoproducts is most important towards next industrial revolution for instance in electronic cooling, heat exchangers, chemical reactors, food processing, medical diagnosis and treatment along with material processing including coating and control of crystal growth and solidification. A prior understanding of flow of nanofluids is very useful for designing any thermal systems and devices.

Literature Review

Huminic and Huminic, 2018, Ali, 2020 and Muneeshwaran et. al., 2021 provided extensive reviews involving preparation, agglomeration and sedimentation of different nanofluids containing single or multiple types of nanoparticles along with the heat-transfer enhancement potential of the nanoparticles. Reviews by Bejan et al., 2004, Kasaeian et. al., 2017 and Khanafer and Vafai, 2019 considered flow through porous structures. The observation of Khaled and Vafai, 2003 regarding flow in numerous tissues of human body as like through porous media makes these reviews even more significant. Kabeelet.al., 2015, M’hamedet.al., 2016, Sheikholeslami and Rokni, 2017, Rashidi et. al.,2017 and Kumar and Subudhi, 2018 reviewed the need of controlling nano flow by employing magnetic field along with scope of applications in biomedical area.

A nano flow analysis calls for a multi-physics approach. Different numerical techniques have been adopted for solving the system of equations. Abu-Nada, 2015 carried out a particle dynamics

simulation study. However, finite-element method by Selimefendigil et al., 2016, Mehryanet al., 2018 and Ghalambaz et al., 2020, lattice-Boltzmann method by Ghasemi and Siavashi, 2017, Sheikholeslami,2017 and Javaherdeh and Najjarnezami, 2018, control-volume method by Nasr et. al., 2006, Oztop et al., 2011, and Mondal et al., 2022 along with its open-foam variation by Baghsaz et al., 2019 are examples of more widely adopted techniques.

Besides the coupling among the conservation of coupled equations for mass, momentum and energy for the flow and heat transfer, Maxwell equations come into play for modeling the coupling of the magnetically induced body force in the momentum conservation equation. A single-phase Newtonian flow model with the momentum conservation principle expressed by Navier-Stokes equation was considered for instance by Sheremet et al., 2016, Ghasemi and Siavashi, 2017, Manna et al., 2021aand 2021b. On the other hand, a two-phase model along with consideration of slip between nanoparticles of 1-100nm size and the base fluid were used by Baghsaz et al., 2019 for the assessment of the extent of particle sedimentation. Ghalambaz et al., 2020adopted a similar approach to capture the non-homogeneous distribution of particles within the base fluid due to the Nano scale forces in a Ferro fluid under external magnetic field.

In presence of permeable pores within the flow domain, Selimefendigil and Chamkha, 2021,Manna et al., 2021aand 2021b modelledthe friction resistance of the pores by Brinkman–Forchheimer–Darcy equation. As pointed out by Lin et al., 2011, Kabeel et al., 2015andPuri and Ganguly, 2014, the flow modelling through porous tissues in animal or human body with external magnetic field is important in the context of medical imaging, tumor treatment and targeted drug delivery. The motions of the bounding surface are insignificant in such cases and the flow resembles the natural convection mode. Mixed or forced convection flow inside a differentially heated cavity with or without the motion of the top lid or side walls provides significant results that are useful in the contexts like air conditioning and material processing.

Besides the governing equations, the other important aspect is the boundary conditions employed for obtaining the solution. Existing numerical studies pertaining to cavities either open only at the top or enclosed on all sides either by stationary or moving walls employ different thermal and magnetic boundary conditions. With reference to some representative numerical research thatare either exploratory in nature or have some specific target applications, these conditions are discussed next. After the discussion, the scope of the problem that has been pursued during the investigation will be elaborated.

Biswas and Manna, 2018 considered constant-temperature heated wall at bottom and cooled walls at two sides along with convective heat flux boundary condition at the open top exposed to a constant-temperature ambient. Besides constant-temperature hot bottom wall and top cold wall,

adiabatic condition was employed by Selimefendigil et al., 2016, Gibanov et al., 2017 and Sheikholeslami,2017 on the side walls. Tiwari and Das, 2007,Al-Rashed et al., 2017, Ghasemi and Siavashi, 2017, Mehryanet al., 2018,Baghsaz et al., 2019, Maghsoudi and Siavashi, 2019, Manna et al., 2021a and b, Selimefendigil and Chamkha, 2021and Mondal et al., 2022imposed constant-temperature hot and cold wall conditions on opposite walls. Biswas et al., 2021 considered half-sinusoid bottom temperature variation, colder constant-temperature side walls and adiabatic or insulated top wall of zero gradient of temperature normal to the wall.

The effects of segmented thermal boundary conditions were investigated by a number of researchers. Nasret. al., 2006 employed constant-temperature cold wall at the top, constant-temperature hot wall at the bottom segment of one side along with vertical motion of the opposite side inducing motion to a single-phase fluid within a cavity closed on all sides. Hussain et al., 2016 considered two discrete segments of hot bottom wall with adiabatic condition on either side along with cold wall at the sides and top. In their analysis, Chamkha et al., 2017 studied the effect of location of a hot segment at the bottom and cold segment at the top wall holding all other walls and part insulated. Jmai et al., 2016analyzed the effect of side walls held hot at the mid segment along with adiabatic conditions in their remaining parts and cold walls at the top and bottom. Al-Rashed et al., 2017 imposed such variation on either the top or bottom segments of a pair of opposite sides of a cubic cavity holding the other pair at adiabatic condition.

In a porous tall cavity, Sheremet et al., 2016 applied constant-temperature cold-wall condition at the open top, hot wall condition at one segment of each the flat bottom and flat sideacross a corner along with their remaining parts and the opposite wavy side wall as adiabatic.Similar boundary conditions were used in a square cavity with all sides flat byMalleswaran and Sivasankaran,2016, by Ahmad et al., 2014 for different tilt angles of the cavity and by Alsabery et al., 2019 with a solid block inserted within the un-tilted cavity. In the studies of Abu-Nada, 2015 and Ismael et al.,2017, only the insulated top-wall condition was different. Corner temperature condition similar to Sheremet et al., 2016was imposed in square cavities by Varol et al.,2009, Oztop et al.,2011and Ismael et al.,2017 along with insulated wall condition everywhere else.

Insulated boundary condition was imposed over the remaining parts of the walls, if not stated in any cavity study mentioned above. Apart from the cubic cavities considered by Al-Rashed et al., 2017 and Sheikholeslami,2017, all other cavity studies mentioned here considered the length in one horizontal direction very long that are designated by their cross section as square, rectangular or hexagonal, say. A possible application of segmented heating could be targeted treatment of a tumor and the segment form would depend on the location and size the tumor. Of course, finer control of the targeted treatment could require additional means like external magnetic field for

sustaining the flow in absence of significant boundary motion or a pump in the lymphatic network. Fritz et al.,2008 mentioned the flow between the lymph capillaries and interstitial space in the body to arise only from muscle pressurization associated with respiration, intestinal peristalsis and skin massaging. On the other hand, wall motion considered in many investigations is a mechanism that induces stronger flow.

The vertical motion of one side wall was analyzed by Abu-Nada, 2015 and Ismael et al.,2017 respectively for a single-phase fluid and CuO-water nanofluid. Biswas and Manna, 2018 considered such motion of both the side walls of an open cavity filled by a single-phase liquidsubjected to gradient of surface tension at the top. Vertical motion of both the side walls was studied by Tiwari and Das, 2007and Chamkha et al., 2017 for Cu-water nanofluid and by Hussain et al., 2016for Al_2O_3-water nanofluid. Horizontal motion of only the top wall was analyzed byOztop et al.,2011and Malleswaran and Sivasankaran, 2016 on a single-phase liquid, Selimefendigil et al., 2016 on CuO-water nanofluid, Gibanov et al., 2017 on Fe_2O_3-water nanofluid and Sheikholeslami, 2017 and Selimefendigil and Chamkha, 2021on Ag-MgO-water nanofluid. For Cu-water nanofluid, Jmai et al., 2016 and Maghsoudi and Siavashi, 2019 studied the effect of horizontal motion of both topmost and bottom walls. The latter investigation pertaining to a porous flow domain exhibited an enhancement of heat transfer for certain nonhomogeneous distribution of pores.

In absence of motion of any wall, the natural-convection of a single-phase fluid was analyzed by many researchers. The study by Nasr et. al., 2006 pertains to flow of air. Predictions by Ahmed et al., 2014 exhibited to increase of both flow of fluid through a porous medium and the heat transfer to increase with increase in wall radiation and pore permeability. The predicted results of Varol et al., 2009 revealed the rate of heat transfer to depend on the tilt angle of the cavity axis with respect to the vertical and the size of the corner heater. During a targeted radiation treatment, the pose of the patient that could be maintained would correspond to the tilt angle with respect to the vertical gravitational field. In absence of significant pumping action or wall movement during many treatments, excitation by an external magnetic field is indeed a viable option of controlling the flow for achieving heating at the desired location with minimal damage to the neighboring areas.

Numerical analyses carried out by Begum et al.,2017 and Biswas et al.,2021pertaining to porous media revealed the possibility of lowering of heat transfer induced by magnetic fields in some situations. The study of Ray and Chatterjee, 2014 held out promises of effective control of the flow characteristics around a round body placed at the center of the cavity exposed to varying magnetic field. The use of magnetic fields over the entire domain of convective systems was initiated long back by Ozoe and Okada, 1989. By realizing an experimental set-up with alternating

magnetic field, Christiansen et al., 2017 showed that magnetic nanofluid could be heated up without inflicting damages to near-by animal tissues. In a numerical study pertaining to an oxygen-filled cavity, Song and Tagawa, 2018 found that positioning of a permanent magnet closer to the wall to yield higher enhancement of heat transfer up to 17.9% in comparison to that without a magnets.

Effects on flow driven by either or both of wall motion and differential heating were studied for external magnetic fields normal and inclined to walls or parts of it with continuous and intermittent variations. Some representative analyses with uniform and continuous magnetic field were accomplished by Ganguly et al., 2004, Oztop et al.,2011, Malleswaran and Sivasankaran,2016andBiswas and Manna,2018for single-phase liquids and by Hussain et al., 2016, Sheremet et al., 2016, Gibanov et al., 2017, Sheikholeslami,2017 and Selimefendigil and Chamkha, 2021for nanofluids.

Of course, the degree of assistance or opposition among thermal, magnetic and wall-driven convection modes were found to depend on their relative angular orientations arising principally from the boundary conditions set. For instance with hot top wall and cold bottom wall, Chamkha et al., 2017 predicted decrease in heat transfer with increase in the ratio of the magnetic force to viscous force referred as Hartmann number. Under such a stable thermal gradient, the setting of convective flow by the upward motion of the vertical side walls seems to be getting opposed by the magnetic convection corresponding to its set field direction. Numerical results of Selimefendigil and Chamkha, 2021 indicated enhancement in heat transfer with increase in the volume fraction of nanoparticles and an effective role of the shape of a triangular porous insert in the local control of heat transfer. With an inclined magnetic field, constant hot temperature across a bottom corner of a cavity with moving top lid, Alsabery et al., 2019, however, found more than 2% Al_2O_3 to be ineffective.

Mehryan et al., 2018 predicted the periodic variation of magnetic field with time along a vertical-wall of a square cavity to be more effective than a uniform variation. From the numerical results of Selimefendigil et al., 2016, the sensitivity of the location of the domain part under the direct application of the magnetic field, the angle of the applied field and Hartmann number were quite evident. Under vertical motion of two vertical side walls, a sinusoidal variation of hot temperature at one side with all other sides insulated and variable magnetic field, the analysis of Fe_2O_3-water ferro-nanofluid fluid by Sheikholeslami and Chamkha, 2016 exhibited the magnetic property of the fluid to help in enhancing the heat transfer and Hartmann number to bring in a reduction. The effect of uniform magnetic field active over one or more segments and inactive over the

surrounding segments were explored in a number of numerical investigations. Over the full domain, any such field gives rise to a nonuniform distribution.

Under a single active segment, Jalil et al., 2013 observed damping of chaotic oscillation. By adjusting the strength and active position of magnetic field, excellent control of heat transportation was predicted under free convection in air-filled differentially heated porous enclosure by Ghasemi et al., 2011 and Geridonmez and Oztop, 2019 and 2020 with horizontal field and by Ghalambaz et al., 2019 with inclined diagonal field. For different positioning and orientation of a permanent magnet smaller in length than any side of the cavity, Szabo and Früh, 2018 predicted emergence of different circulation patterns, local heating and a minima in the global heat transfer.

The effects of nonuniform magnetic activation in single segment over a part of a cavity wall were studied in the context of nanofluids as well. In a differentially-heated cubic cavity filled with carbon-nanotubes in water surrounded by stationary walls on all sides, Al-Rashed et al., 2018 predicted locational control of heating depending on the application of the magnetic field normal to the top or bottom segment of one vertical wall. With respect to no magnetic field applied in a square tilted cavity with stationary walls, Mondal et al., 2022 predicted nearly 15% and 30% reduction in overall heat transfer with variation in the tilt angle respectively under the whole-domain and single-segment magnetic fields. In recent studies, Manna et al., 2021a and b explored the application of magnetic field in multiple segments.

Scope of Work

A survey of the existing research status detailed above has motivated the plan of the numerical study reported here. Both the hot wall condition and the external magnetic field normal to the wall has been imposed in the middle segment of the side walls in a square cavity with stationary walls in both tilted and un-tilted orientations. Nanoparticles of Cu and Al_2O_3 with water as the base fluid has constituted the nanofluid. Mathematical model used in the study is detailed in Chapter 2. In Chapter 3, the solution method, its validation and numerical results are discussed. Conclusions and scope of future studies are summarized in Chapter 4.

CHAPTER 2: MATHEMATICAL MODELING

Problem definition

An analysis of flow of a hybrid Cu-Al_2O_3-water nanofluid has been undertaken here in a two-dimensional porous square cavity with $L = H = 1$, as shown in Fig. 1. A pair of adiabatic opposite walls are considered. These walls are horizontal in the un-tilted cases. Each of the other two walls has a heater length L_{hl} equal to L_{hr} maintained at a constant high temperature T_h in the middle segment between two colder segments at T_c. This heating type is mentioned hereafter as **MM type**. Over the active part, the magnetic field has uniform strength B.

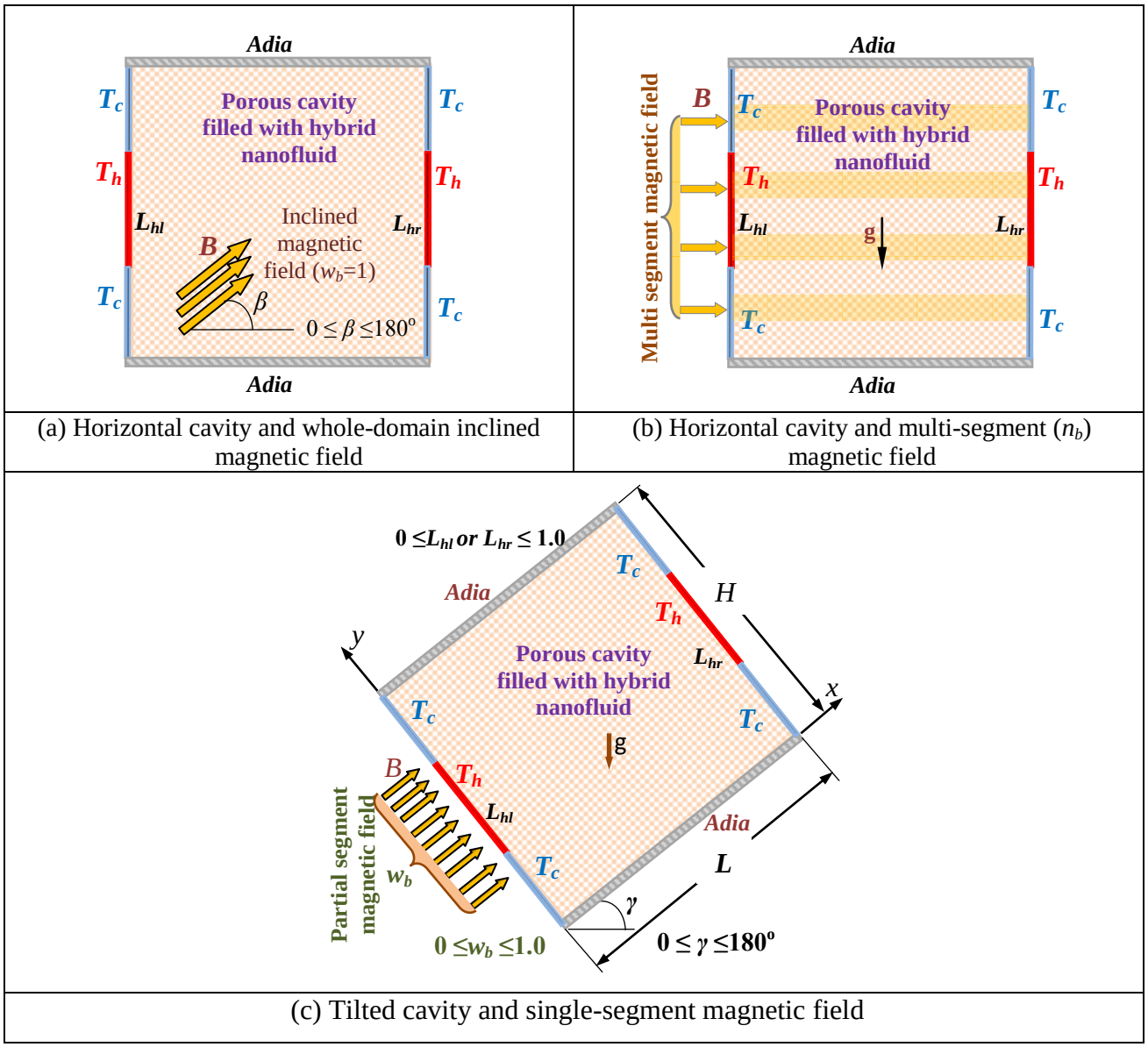

(a) Horizontal cavity and whole-domain inclined magnetic field

(b) Horizontal cavity and multi-segment (n_b) magnetic field

(c) Tilted cavity and single-segment magnetic field

Fig. 1: Mid-segment heating of a facing pair of walls in a porous square cavity filled with a hybrid nanofluid for different cavity orientations and magnetic fields.

In Fig. 1a, the field is active over the whole domain of the cavity across the vertical side walls at an angle β with respect to the horizontal walls. Segmented fields normal to a pair of opposite walls are considered in Figs. 1b and 1c. A single segment is employed across the middle of a pair of tilted side walls in the case represented by Fig. 1b with angle of tilt given by γ for all the side walls with respect to the horizontal direction. There are four equally spaced similar segments across the vertical side walls in case of Fig. 1c. These vertical walls of an un-tilted cavity are shown subjected to four discrete segments, referred also as partial segments. The practical realization of such segmented forms of magnetizing fields may be prepared by appropriate electrical coil winding.

Mathematical formulation and model simulation

Governing Equations

Mathematical modeling of flow of a nanofluid through a porous structure under thermo-magnetic field is quite challenging due to various multi-physics coupling like flow dampening in porous medium, temperature-induced buoyancy and magnetic force on nanoparticles. A steady flow analysis has been taken up in order to keep the analysis simple. By considering a small concentration ≤2% of nanoparticles of copper and alumina assuming to be of uniform spherical diameter of ~1 nm homogeneously dispersed in water, a single-phase flow analysis has been performed for a fluid of Prandtl number Pr equal to 5.83. Of course, the sedimentation and agglomeration of particles have been ignored. The flow is presumed as Newtonian, incompressible and laminar and the effect of viscous dissipation has been neglected. Brinkman-Forchheimer-Darcy model has been invoked to study the flow through a homogeneous material of uniform pores in local thermal equilibrium between the solid materials and the fluid. Boussinesq approximation has been employed in order to take care of the buoyant body force arising from the gradient of fluid density due to the variation of temperature. Maxwell model of magnetic induction for an electrically conducting fluid, only Lorentz force has been assumed important. For simulating flow of low magnetic Reynolds number and low volume fraction of nanoparticles, Joule heating and Hall effect have been neglected. Thus, the governing equations are written as

$$\frac{\partial U}{\partial X}+\frac{\partial V}{\partial Y}=0 \tag{1}$$

$$\frac{1}{\varepsilon^2}\left(U\frac{\partial U}{\partial X}+V\frac{\partial U}{\partial Y}\right)=-\frac{\rho_f}{\rho}\frac{\partial P}{\partial X}+\frac{\nu\,\mathrm{Pr}}{\nu_f\varepsilon}\left(\frac{\partial^2 U}{\partial X^2}+\frac{\partial^2 U}{\partial Y^2}\right)-\left(\frac{\nu\,\mathrm{Pr}}{\nu_f\,\mathrm{Da}}+\frac{F_c\sqrt{U^2+V^2}}{\sqrt{\mathrm{Da}}\;\varepsilon^{3/2}}\right)U$$
$$-\frac{\rho_f}{\rho}\frac{\sigma}{\sigma_f}\lambda_B\mathrm{Ha}^2\,\mathrm{Pr}(V\sin\gamma\cos\gamma-U\sin^2\gamma) \tag{2}$$

$$\frac{1}{\varepsilon^2}\left(U\frac{\partial V}{\partial X}+V\frac{\partial V}{\partial Y}\right)=-\frac{\rho_f}{\rho}\frac{\partial P}{\partial Y}+\frac{\nu\,\mathrm{Pr}}{\nu_f\varepsilon}\left(\frac{\partial^2 V}{\partial X^2}+\frac{\partial^2 V}{\partial Y^2}\right)-\left(\frac{\nu\,\mathrm{Pr}}{\nu_f\,\mathrm{Da}}+\frac{F_c\sqrt{U^2+V^2}}{\sqrt{\mathrm{Da}}\,\varepsilon^{3/2}}\right)V$$
$$-\frac{\rho_f}{\rho}\frac{\sigma}{\sigma_f}\lambda_B\mathrm{Ha}^2\,\mathrm{Pr}(U\sin\gamma\cos\gamma-V\cos^2\gamma)+\frac{(\rho\zeta)}{\rho\zeta_f}\mathrm{Ra_m}\frac{\mathrm{Pr}}{\mathrm{Da}}\theta \quad (3)$$

$$\left(U\frac{\partial\theta}{\partial X}+V\frac{\partial\theta}{\partial Y}\right)=\frac{\alpha}{\alpha_f}\left(\frac{\partial^2\theta}{\partial X^2}+\frac{\partial^2\theta}{\partial Y^2}\right), \quad (4)$$

in terms of non-dimensional rectilinear system (X, Y), the corresponding velocity components U and V, pressure P and temperature θ corresponding to the dimensional variables x, y, u, v, p and T related by

$$(X,Y)=(x,y)/H;\,(U,V)=(u,v)H/\alpha_f;$$
$$\theta=(T-T_c)/(T_h-T_c);\,P=(p-p_a)H^2/\rho_f\alpha_f^2, \quad (5a)$$

along with

$$\mathrm{Pr}=\frac{\nu_f}{\alpha_f};\,\mathrm{Da}=\frac{K}{H^2};\,F_c=\frac{1.75}{\sqrt{150}};$$
$$\mathrm{Ra_m}=\frac{g\zeta_f(T_h-T_c)KH}{\nu_f\alpha_f};\,\mathrm{Ha}=BH\sqrt{\sigma_f/\mu_f}, \quad (5b)$$

where the dimensionless numbers $\mathrm{Ra_m}$, Pr, Ha, Da and F_c correspond to Darcy–Rayleigh, Prandtl, Hartmann and Darcy numbers along with Darcy-Forchheimer coefficient respectively.

The boundary conditions are chosen as:

$\theta = 1$ and $\theta = 0$ for the heat source and heat sink in either side walls,

$\partial\theta/\partial Y = 0$ _top and bottom adiabatic walls, and

$U = V = 0$ no-velocity for all walls; no slip conditions.

Thermo-physical properties of the base fluid, Cu and Al_2O_3 nanoparticles given in Table 1 have been taken from Biswas *et al.*, 2021a. Tables 2 and 3 provide the mixture rules adopted in this study that are due to Brinkman, 1952, Maxwell, 1904 and Suresh et al., 2012 all corresponding to volume fractions φ composed of those for nanoparticles of Cu and Al_2O_3 as

$$\varphi=\varphi_{Al_2O_3}+\varphi_{Cu} \quad (6)$$

For estimation of heat transportation rate from the hot source wall, the average Nusselt number (Nu) is computed from the resolved temperature field through the subsequent expression as

$$\mathrm{Nu}=\frac{k}{k_f}\int_0^1\left(-\frac{\partial\theta}{\partial X}\bigg|_{X=0,1}\right)dY \quad (7)$$

Table 1: Thermo-physical properties of water and nanoparticles (Cu, Al_2O_3) at 300 K (Biswas et al., 2021a)

Physical properties	**Water**	**Cu**	**Al_2O_3**
Specific heat c_p ($Jkg^{-1}K^{-1}$)	4179	385	765
Thermal conductivity k ($Wm^{-1}K^{-1}$)	0.613	401	40
Density ρ (kgm^{-3})	997.1	8933	3970
Thermal diffusivity $\alpha = k/(\rho c_p)$ (m^2s^{-1})	1.47×10^{-7}	1.11×10^{-4}	131.7×10^{-7}
ζ (K^{-1})	21×10^{-5}	1.67×10^{-5}	0.85×10^{-5}
Viscosity μ ($kgm^{-1}s^{-1}$)	9.09×10^{-4}	-	-

Table 2: Correlations for effective physical properties of hybrid nanofluid (Brinkman, 1952 and Maxwell, 1904)

Effective physical properties	**Correlations for hybrid nanofluid**
Density	$\rho = (1-\varphi)\rho_f + \varphi\rho_s$, where $\varphi\rho_s = \varphi_{Al_2O_3}\rho_{Al_2O_3} + \varphi_{Cu}\rho_{Cu}$
Specific heat capacity	$(\rho c_p) = (1-\varphi)(\rho c_p)_f + \varphi(\rho c_p)_s$, where $\varphi(\rho c_p)_s = \varphi_{Al_2O_3}(\rho c_p)_{Al_2O_3} + \varphi_{Cu}(\rho c_p)_{Cu}$
Thermal expansion coefficient	$(\rho\zeta) = (1-\varphi)(\rho\zeta)_f + \varphi(\rho\zeta)_s$, where $\varphi(\rho\zeta)_s = \varphi_{Al_2O_3}(\rho\zeta)_{Al_2O_3} + \varphi_{Cu}(\rho\zeta)_{Cu}$
Thermal conductivity	$k = k_f\left[\frac{(k_s+2k_f)-2\varphi(k_f-k_s)}{(k_s+2k_f)+\varphi(k_f-k_s)}\right]$, where $\varphi k_s = \varphi_{Cu}k_{Cu} + \varphi_{Al_2O_3}k_{Al_2O_3}$
Electrical conductivity	$\sigma = \sigma_f\left[1+\frac{3(\sigma_s/\sigma_f-1)\varphi}{(\sigma_s/\sigma_f+2)-(\sigma_s/\sigma_f-1)\varphi}\right]$, where $\varphi\sigma_s = \varphi_{Cu}\sigma_{Cu} + \varphi_{Al_2O_3}\sigma_{Al_2O_3}$
Thermal diffusivity	$\alpha = k(\rho c_p)^{-1}$
Viscosity	$\mu = \mu_f(1-\varphi)^{-2.5}$

Table 3: Viscosity and thermal conductivity of hybrid nanofluid (Suresh et al., 2012)

φ (%)	φ_{Cu} (%)	$\varphi_{Al_2O_3}$ (%)	k ($Wm^{-1}K^{-1}$)	μ ($kgm^{-1}s^{-1}$)
0.1	0.0038	0.0962	0.619982	0.000972
0.33	0.0125	0.3175	0.630980	0.001098
0.75	0.0285	0.7215	0.649004	0.001386
1.0	0.0380	0.9620	0.657008	0.001602
2.0	0.0759	1.9241	0.684992	0.001935

For visualizing the multi-physical transport phenomena in presence of partially activated magnetizing fields, the contours of streamlines, heatlines and isotherms have been plotted. The heatline contours demonstrate the dynamics of heat flux corridors within the flow field by collectively merging convection and conduction heat-fluxes. Heat function (Π) (Biswas *et al.,* 2018; Biswas *et al.,* 2021a; Manna *et al.,* 2021) has been calculated from the energy balance in the steady-state situation from the relations

$$-\frac{\partial \Pi}{\partial X} = V\theta - \frac{k}{k_f}\frac{\partial \theta}{\partial Y} \text{ and } \frac{\partial \Pi}{\partial Y} = U\theta - \frac{k}{k_f}\frac{\partial \theta}{\partial X} \tag{8}$$

As the isotherm patters depict the temperature distribution over the entire flow domain, the flow distribution is captured by streamlines, each having a constant value of stream function ψ that is defined as (Manna *et al.,* 2021)

$$-\frac{\partial \psi}{\partial X} = V \text{ and } \frac{\partial \psi}{\partial Y} = U \tag{9}$$

Of course, prior to extracting these functions, the solution for flow velocity and the temperature distribution within the domain should be obtained,

Solution procedure

The outcomes of the computational flow domain are acquired by resolving the coupled transport nondimensional governing equations (1)-(4) by means of in-house developed computation code involving finite volume method (FVM). Nonlinear partial differential equations are linearized and discretized by adopting the second order central and third order upwind differencing schemes for diffusion and advection terms. The discretized equations are solved iteratively following the SIMPLE algorithm (Patankar, 1980; Lewis *et al.*, 2004; Nithiarasu *et al.*, 2016) using tri-diagonal matrix algorithm (TDMA) and alternate direction implicit (ADI) sweep. A flowchart shown in Fig. 2 describes the computation procedure. The convergence of the solution is established with progressive minimization of the variables and the continuity mass defect below 10^{-8} and 10^{-10} respectively. The same in-house code were utilized were employed earlier in multiphysics situations pertaining to free convection, mixed convection, Marangoni convection, porous medium, nanofluids, hybrid nanofluids and magnetic fields (Biswas*et al.,* 2021a; Biswas *et al.*, 2021b; Biswas*et al.,* 2021c). In their work, a number of successful validation studies were presented. Hence, no validation study has not been carried out for the work undertaken here. Through a grid independence study based on nonuniform meshing presented next, the appropriate number of grid lines has been selected for executing a detailed parametric study.

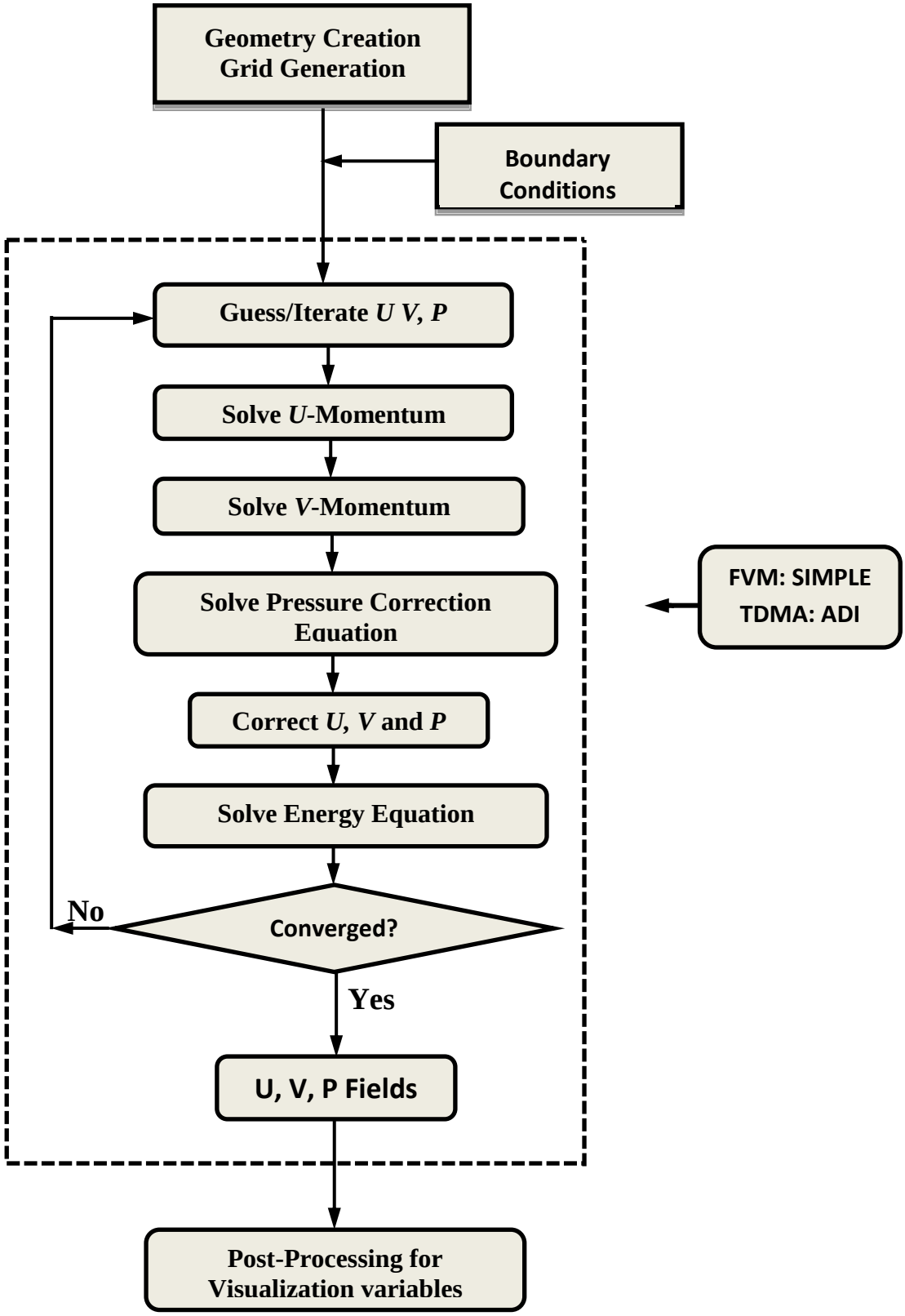

Fig.2: Detail flowchart representing various steps of the whole computation process.

Grid independent study

The grid independent study for the computational domain of current problem is evaluated in hybrid nanofluid packed porous cavity with MM type heating in an un-tilted square cavity with Da = 10^{-3}, ϕ = 0.1%, ε = 0.8, Ha = 50, w_b = 1, β = 0 and γ = 0. A number of non-uniform grid structures with 70×70, 100×100, 130×130, 160×160, 190×190 and 220×220 spaces have been used for different Darcy–Rayleigh number introduced in (5b). For these grids, Table 4 lists the average values of Nusselt number computed by using (7). A typical nonuniform grid structure is shown in Fig. 3. Beyond the 100×100 grid, the successive change of Nu between the respective cases of immediately more refined grid remains less than 1%. In fact between the 190×190 and 220×220 grids, the changes are insignificant. Keeping the computational time in mind, the 160×160 grid has been chosen for the detailed study described in the next chapter.

Table 4: Average Nusselt number (Nu) at Da = 10^{-3}, Ha = 50, ε = 0.8, ϕ = 0.1%, w_b = 1, β = 0 and γ = 0 for Case MM type segmental heater position

Ra_m	70×70	100×100	130×130	160×160	190×190	220×220
10	6.817	6.898(1.17%)	6.958(0.86%)	6.968(0.13%)	7.011(0.62%)	7.018(0.10%)
100	6.831	6.902(1.04%)	6.960(0.83%)	6.994(0.48%)	7.061(0.95%)	7.065(0.07%)
1000	7.786	7.866(1.01%)	7.901(0.45%)	7.920(0.23%)	7.923(0.05%)	7.936(0.16%)
10000	11.868	11.983(0.96%)	12.009(0.21%)	12.028(0.16%)	12.114(0.71%)	12.122(0.07%)

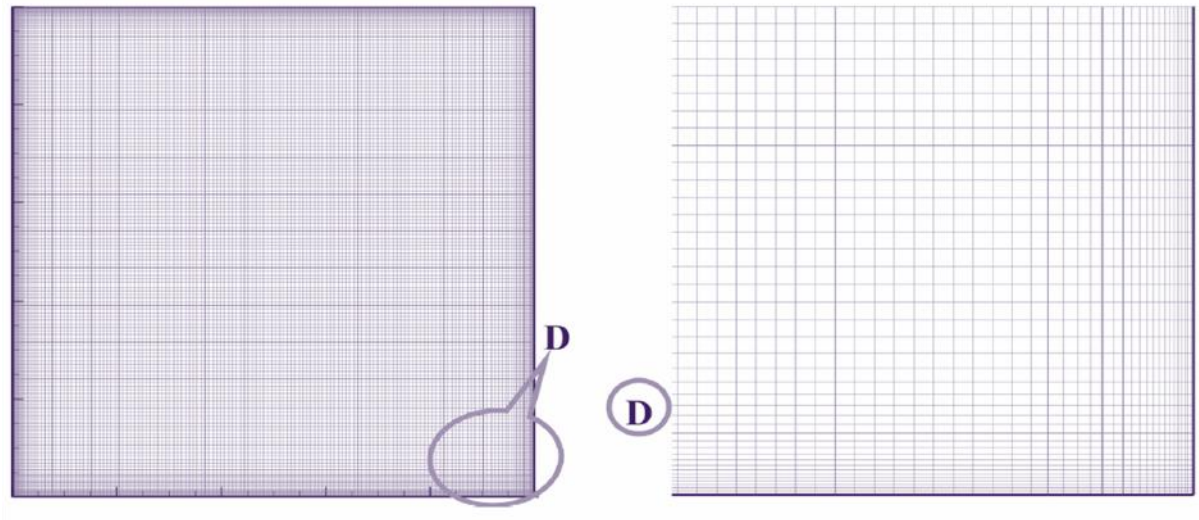

Fig. 3: Detail view of grid refinement structure in computational domain

CHAPTER 3: RESULTS AND DISCUSSION

Overview

A numerical study is taken up here at the constant setting of other parameters for different heater arrangements, Darcy-Rayleigh number Ra_m equal to 10, 10^2, 10^3, 10^4, Darcy number Da equal to 10^{-1}, 10^{-2}, 10^{-3}, 10^{-4}, 10^{-5}, porosity index ε equal to 0.1, 0.3, 0.4, 0.6, 0.8, 1.0, volume fraction of hybrid nanoparticles ϕ equal to 0, 0.1%, 0.33%, 0.75%, 1%, 2% and Hartmann number Ha equal to 0 (no field), 10, 30, 50, 70. Thermo-fluid effects have been examined in terms of the flow velocity, temperature, heat flux pattern and heat transport. These have been captured by contours of streamlines, isotherms, heatlines, average and local numbers Nu and Nu_l. In Parts 1 and 2, the cases of constant and variable magnetic fields are respectively investigated.

Part 1: Constant magnetic field with Ha equal to 50 and whole-domain magnetic field with w_b equal to 1.0

a) Facing and staggered arrangements of two different constant-temperature pairs on side walls

Results are presented for $Ra_m=10^3$, $Da=10^{-2}$, $\varepsilon=0.8$ and $\phi=0.1\%$ are presented in Figs. 4 to 8 under no magnetic excitation for different cases listed in Table 5. A comparative analysis of L, R and MM cases is illustrated in Fig. 4. As expected the cases of L and R with only the full left and right wall heated respectively, the contours and the circulation patterns in one case evolve as the mirror image of the other. Moreover, the average Nu is identical in both the cases. These aspects clearly reveal the strength of the computational algorithm. As the fluid near the hot wall is heated up, a tendency of it to rise by displacing the adjacent side layer of relatively colder fluid develops. Near the cold wall, the increased fluid density gives rise to a downward flow that effectively causes the flow to circulate in a single loop.

Table 5: Possible combinations study on hot wall position.

Combinations	**Descriptions**
L	Full length Left wall is hot
R	Full length Right wall is hot
TT	Top - Top half length sidewalls are hot
MM	Middle - Middle half length sidewalls are hot
BB	Bottom - Bottom half length sidewalls are hot
TM	Top - Middle half length sidewalls are hot
TB	Top - Bottom half length sidewalls are hot
MB	Middle - Bottom half length sidewalls are hot

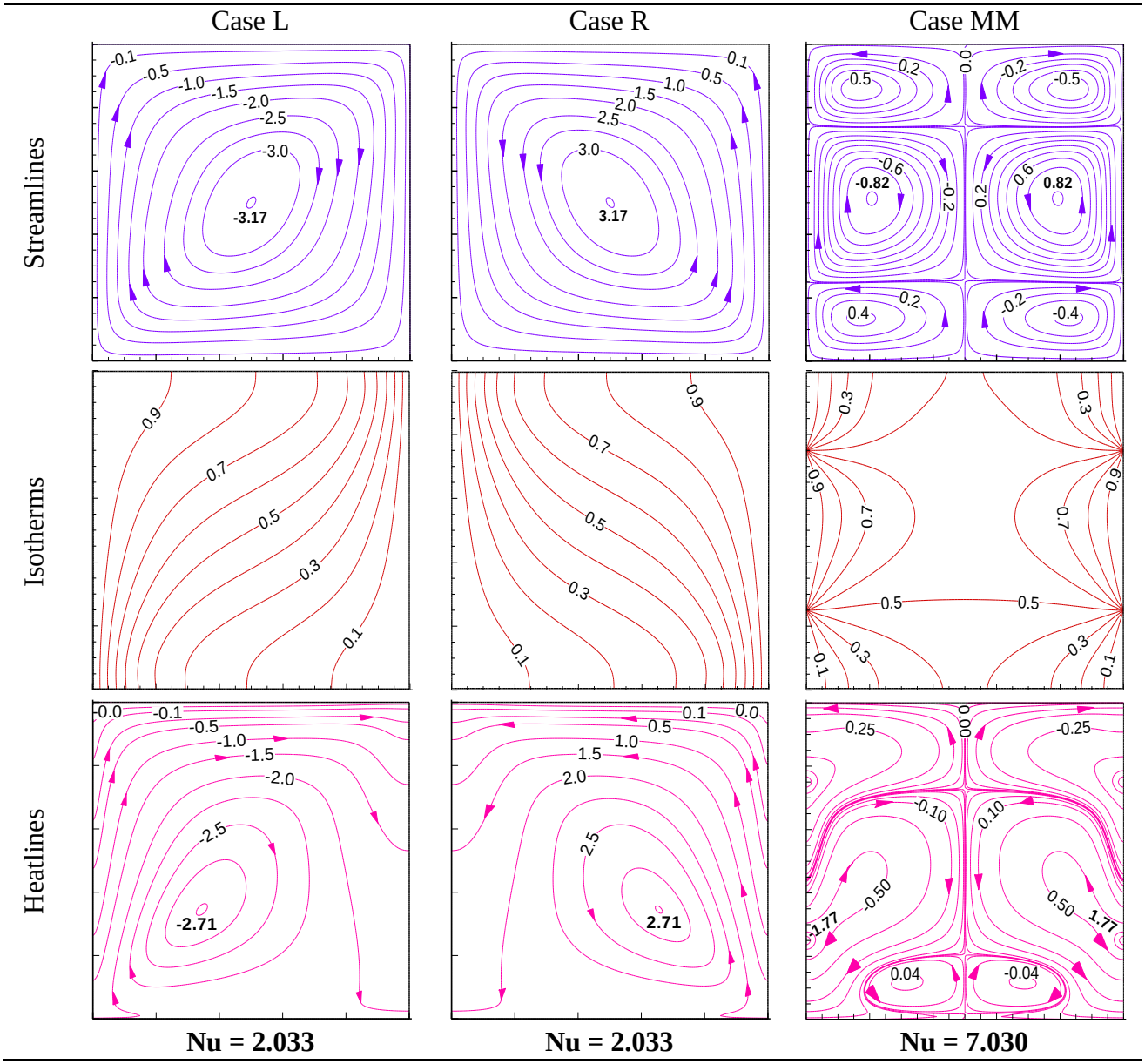

Fig. 4: Thermo-fluid structures through streamlines (top panel) isotherms (mid panel) and heatlines (bottom row) at $Ra_m = 10^3$, Ha = 50, $Da = 10^{-2}$, $w_b = 1$, $\phi = 0.1\%$, $\gamma = 0$ and $\beta = 0$ under L, R and MM arrangements. MM type shows maximum Nu.

In view of lower fluid density at higher temperature, the proportion of the colder fluid is expected to progressively increase in the downward direction. This feature is evident from the upward and downward bending of the isotherms away from the hot and cold walls respectively. Hence, the temperature gradient across the isotherms near the hot and cold walls decreases in the upward and downward directions respectively. Driven by the variation of density inversely to the vertical gradient of the fluid temperature, the convection current keeps retarding during the ascent near the hot wall and descent near the cold wall. The flow divergence associated with the continuity of the retarding fluid explains the numerically predicted skewed circulation pattern.

Over the region of the convection-dominated heat transfer near most of the constant-temperature walls, the heatlines emanating from the hot wall and terminating on the cold wall exhibit close alignment with the streamlines. However near the corners with higher packing of the isotherms, the domination of conduction over convection makes the heat line to get aligned closer to normal of the isotherms. From the streamline directions, the heatlines near these corners show substantial deviations so as to emanate from the hot wall and terminate on the cold wall. Such terminations of some heatlines together with their expected nearly parallel nature near the adiabatic walls gives rise to a bunch of circulatory heatlines without any contact with any wall.

The symmetric pattern of the MM case in Fig. 4 with $L_{hl} = L_{hr} = 0.5L$ about the vertical line of symmetry is consistent with the imposed boundary conditions. In each half of symmetry, the circulation patterns appear to remain more or less contained along the vertical expanse of the respective walls. In the middle segment, the circulation pattern is clearly driven by the density gradient causing ascent of the fluid near the hot wall and descent near the vertical plane of symmetry having the minimum temperature for being equally away from the walls on either side. In the cold segments, the circulation patterns appear to be dragged by the viscous flow in the adjacent parts of the hot segment with the streamlines there and the adjacent cold zones revealing identical flow direction. The most significant finding for the segmental MM heating is enhancement of the overall heat transfer over both the L and R cases by **245.79 %** reflected by the corresponding Nu.

In Fig. 5, the same MM case as above is compared with two other cases of identical heater lengths and vertical plane of symmetry designated in Table 5 as TT and BB. The high concentration of the streamlines near each hot and cold junction and their diverging progression obliquely away from this region is consistent with the highest density gradient here. Since the vertical mid plane is equally away from both the hot walls, the minimum temperature is attained here causing a decent of the flow on its either side. Thus a pair of counter-rotating circulation patterns develop in the middle segment. On each of the top and bottom cold-wall segments, the viscous action of the nearly horizontal parts of the respective bordering flow in the middle segment gives rise to a pair of counter-rotating circulation loops. Such viscosity-driven pair of counter-rotating pairs of symmetric circulation loops evolve only in the bottom or top segments in the TT and BB cases respectively. Hence, these cases have two pairs of loops, whereas the MM case has three pairs.

Contrasting the symmetric arrangements with facing constant-temperature wall pairs, the cases TM, TB and MB of Table 5 presented in Fig. 6 have facing wall of opposite types. In the cases involving heating in the middle over half of one side wall is associated with equal span of lower

temperature at the top and the bottom. On the other hand, the sides without mid-segmented heating has each half of opposite constant-temperature pair. As expected, no symmetry about the vertical mid plane has emerged from the upward rise of flow along the hot wall segments or hotter fluid side and decent along the cold wall segments or colder fluid side. Corners with either low or high temperature gradients associated respectively with divergence and convergence among the streamlines approaching the respective corners are evident like in case of Fig. 4. Higher Nu in the MM case than the two other symmetric cases of TT and BB apparent in Fig. 7 for all Ra_m is indeed due to higher mixing entailed by one more pair of circulation zones.

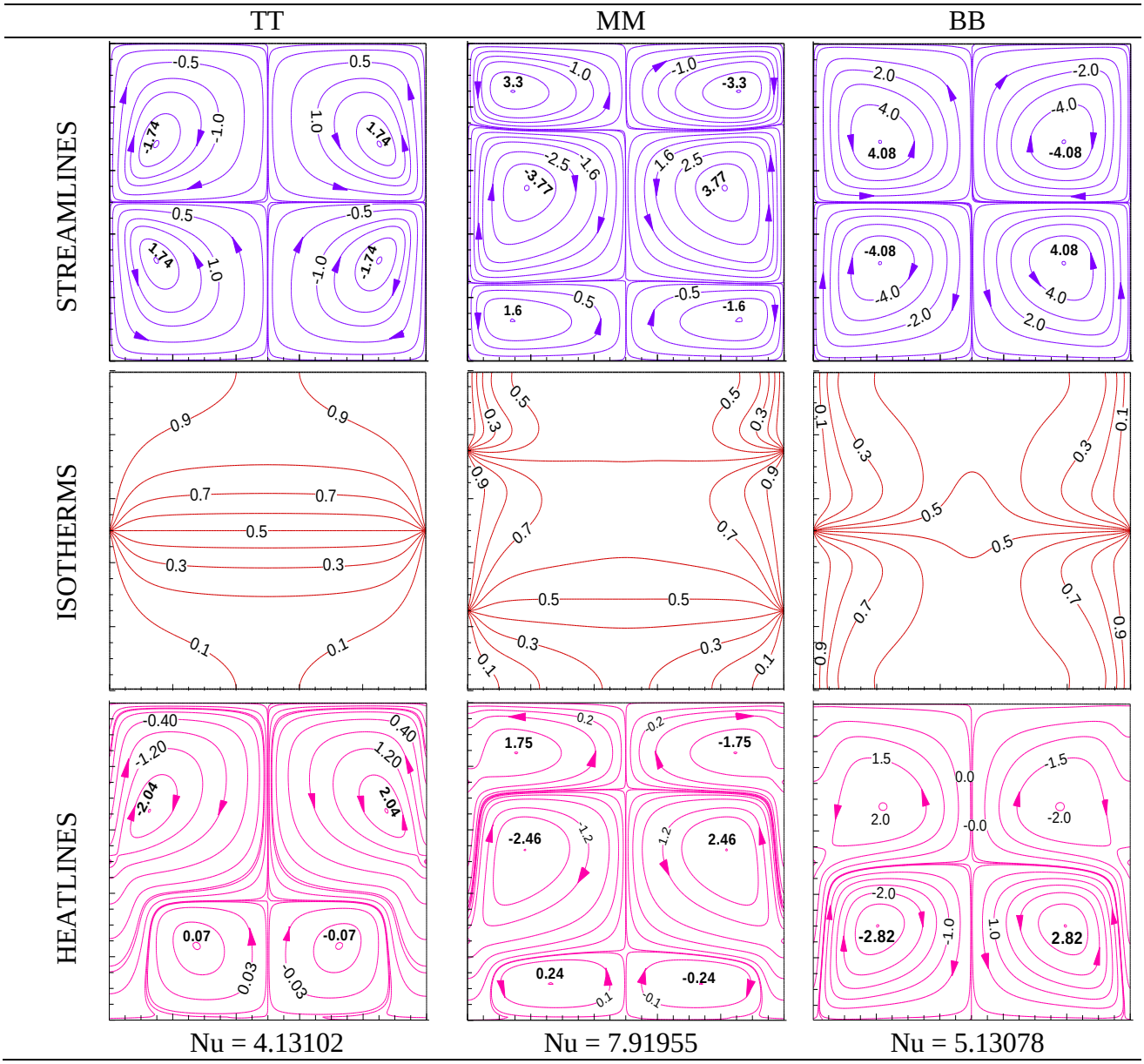

Fig. 5: Thermo-fluid contours with identical constant-temperature conditions imposed on facing side-wall segments at $Ra_m = 10^3$, Ha = 50, Da = 10^{-3}, ϕ = 0.1%.

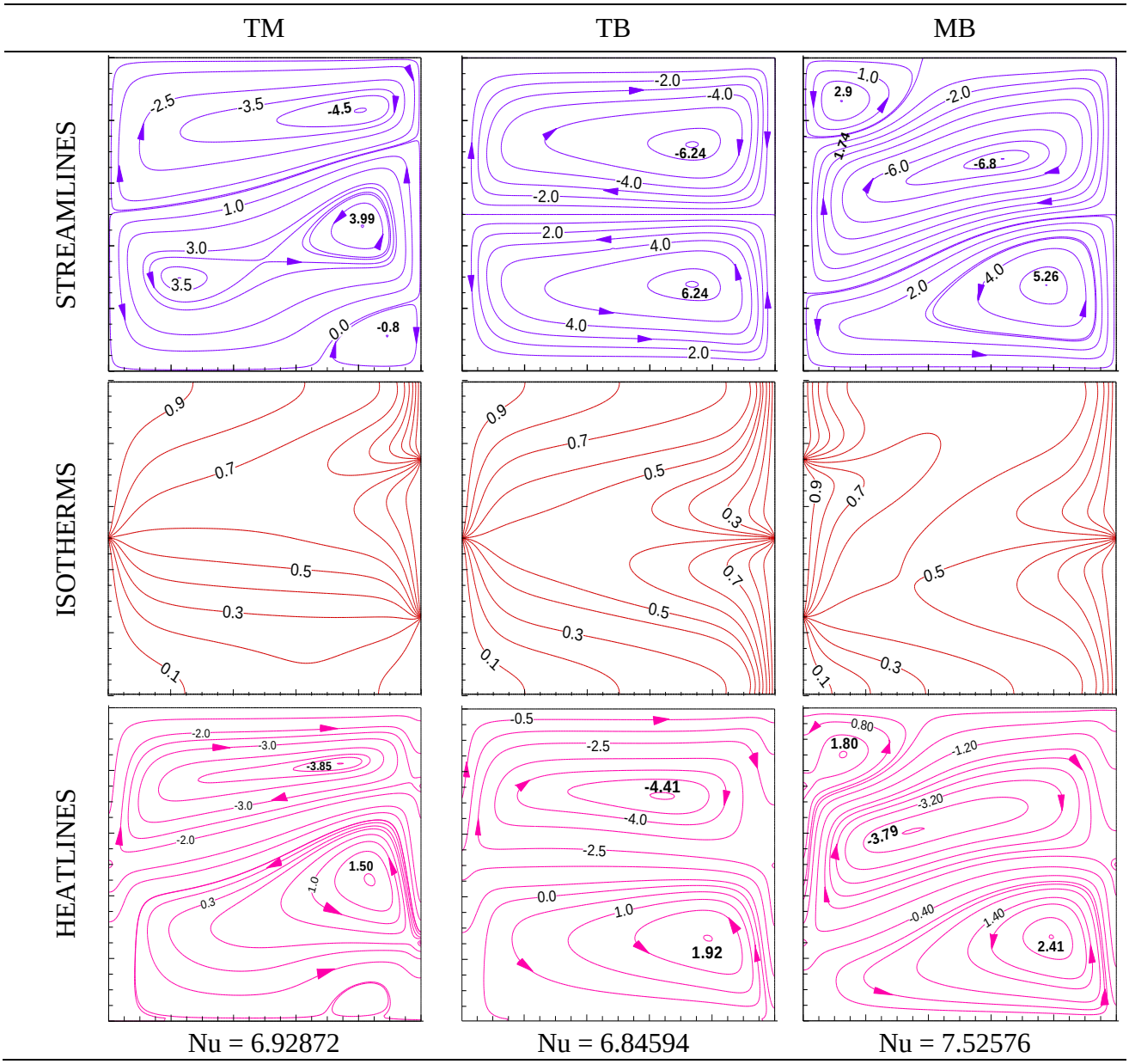

Fig. 6: Thermo-fluid contours with opposite constant-temperature conditions imposed on facing side-wall segments of an un-tilted square cavity at $Ra_m = 10^3$, Ha = 50, Da = 10^{-3}, ϕ = 0.1%.

In the TT case, the isotherms in Fig. 5 reveal nearly equal temperature in each corner close to the corresponding imposed wall temperature-condition. Away from the corner, the temperature increases towards the top. The corresponding decrease of density makes the system thermally passive. In the BB case, however the presence of hot lighter fluid towards the bottom as apparent from the isotherms makes the system thermally active. Higher stream function value in this case is also a testimony to the invigorated flow and higher Nu in comparison to the TT case.

The highest local heat transfer is predicted in Fig. 7 near each of the junction points of two different temperatures presumably due to the convective augmentation associated with the highest temperature gradient within the fluid. Only over the hotter temperature length mentioned as source

in the figure, the variation of local Nusselt number is shown. An interesting observation of Fig. 7 is the best heat transfer enhancement provided by MM arrangement up to Ra_m of 1000. This can be attributed to higher number of circulation loops leading to better mixing. In case of Ra_m of 10000, however, higher enhancements are predicted by the cases of asymmetric heating arrangements. A greater length of colder fluid lying above hotter fluid make these cases susceptible to instabilities and the corresponding greater mixing. Clearly, the present study indicates the most effective wall heating arrangements for different Ra_m along with the physical explanations of the thermo-fluid features in the different cases.

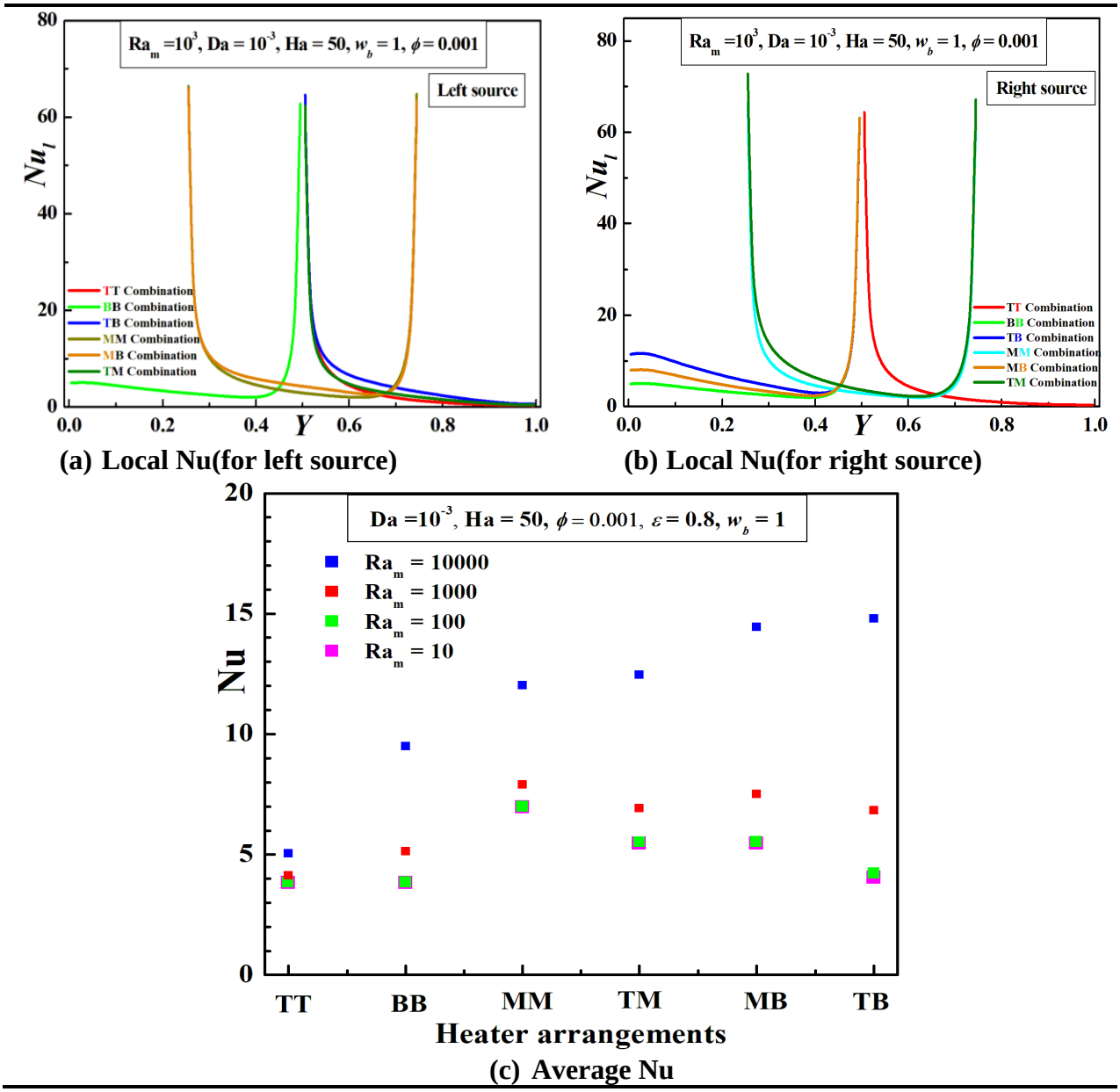

Fig. 7: Heat transfer in terms of local Nu and Nu average for different combinations of segmental heater in side walls at $Ra_m = 10^3$, Ha = 50, Da = 10^{-3}, ϕ = 0.1%.

b) Different heater sizes

The effect of different heater sizes on the middle segment of the facing walls are brought out through Figs. 8 ad 9 corresponding to the different cases listed in Table 6 for $Ra_m = 10^3$, Ha = 50, $Da = 10^{-3}$, $\varphi = 0.1\%$, $\varepsilon = 0.8$, and $\gamma = 0^o$. Extended from the top to the bottom temperature junctions on the side wall with smaller heater, a streamline is seen to enclose circulatory streamlines ascending along the side closer to the hot wall. Below this circulation zone, another such is evident descending downward near the cold wall. This zone is seen embedded within another circulatory pattern ascending near the longer heater in the middle segment and descending down the colder walls on the opposite side wall.

L_{hl}/L_{hr} = 0.6/0.4 [Case 5]	L_{hl}/L_{hr} = 0.4/0.6 [Case 6]	L_{hl}/L_{hr}= 0.8/0.2 [Case 3]	L_{hl}/L_{hr} = 0.2/0.8 [Case 4]
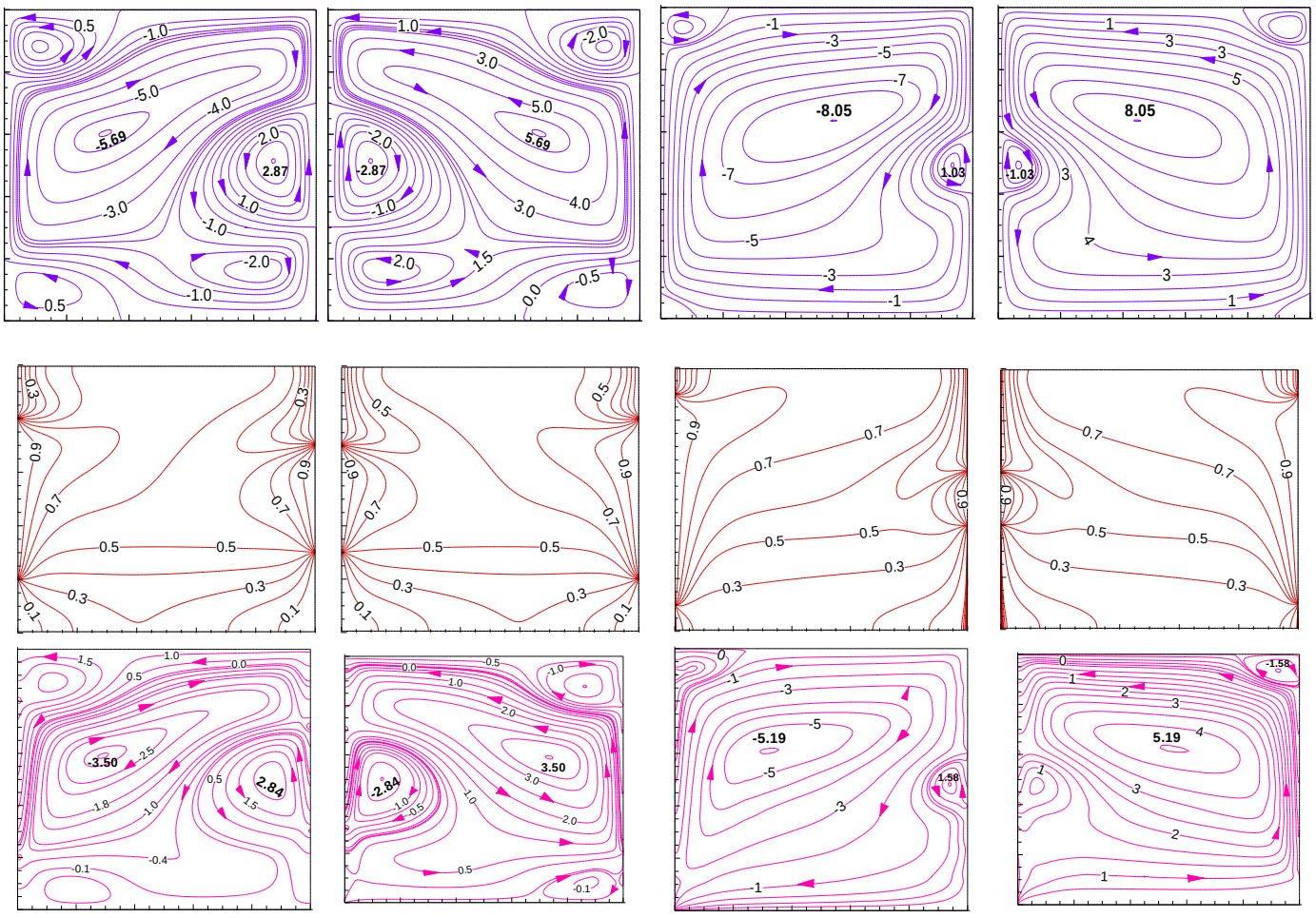			
Nu = 9.114	Nu = 9.114	Nu = 9.657	Nu = 9.657

Fig. 8: Contour structures in for different sizes of segmental heater in either side walls of an un-tilted square cavity at $Ra_m = 10^3$, Ha = 50, $Da = 10^{-3}$, $\phi = 0.1\%$.

Table 6: Combination of full left or right-wall heating and different sizes of MM heater

Case study	Descriptions	Symbol
Case 1, L	Left wall heater size = H, No heater at right wall	$L_{hl} = H$, $L_{hr} = 0$
Case 2, R	No heater at left wall, Right wall heater size = H	$L_{hl} = 0$, $L_{hr} = H$
Case 3	Middle centered left heater size = 0.8H Middle centered right wall heater size = 0.2H	$L_{hl} = 0.8H$ $L_{hr} = 0.2H$
Case 4	Middle centered left heater size = 0.2H Middle centered right heater size = 0.8H	$L_{hl} = 0.2H$ $L_{hr} = 0.8H$
Case 5	Middle centered left heater size = 0.6H Middle centered right heater size = 0.4H	$L_{hl} = 0.6H$ $L_{hr} = 0.4H$
Case 6	Middle centered left heater size = 0.4H Middle centered right heater size = 0.6H	$L_{hl} = 0.4H$ $L_{hr} = 0.6H$
Case 7	Middle centered right and left heater size = 0.5H	$L_{hl} = L_{hr} = 0.5H$

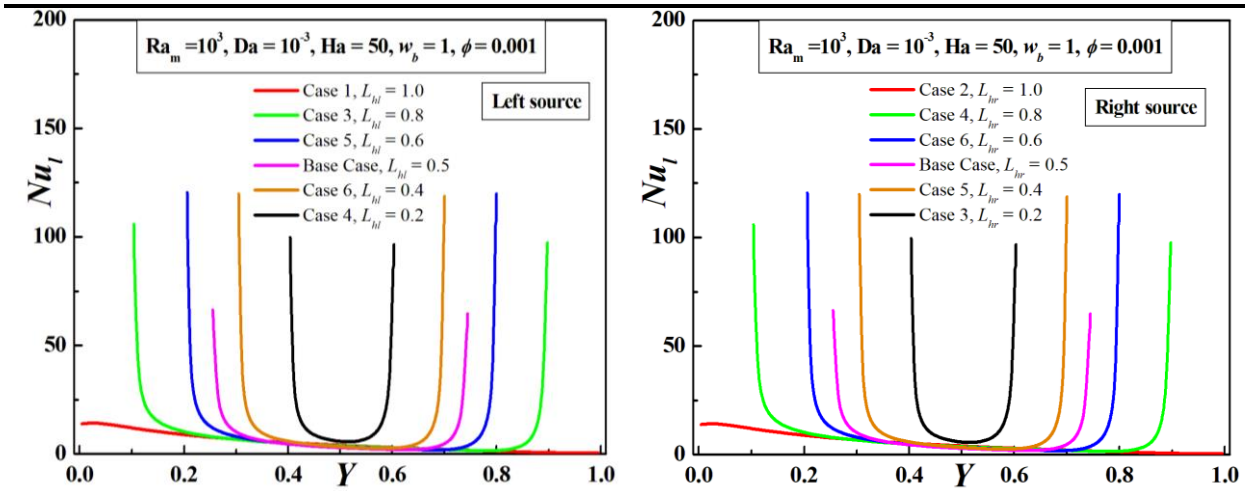

a) Local Nu at left source for all heater lengths b) Local Nu at right source for all heater lengths

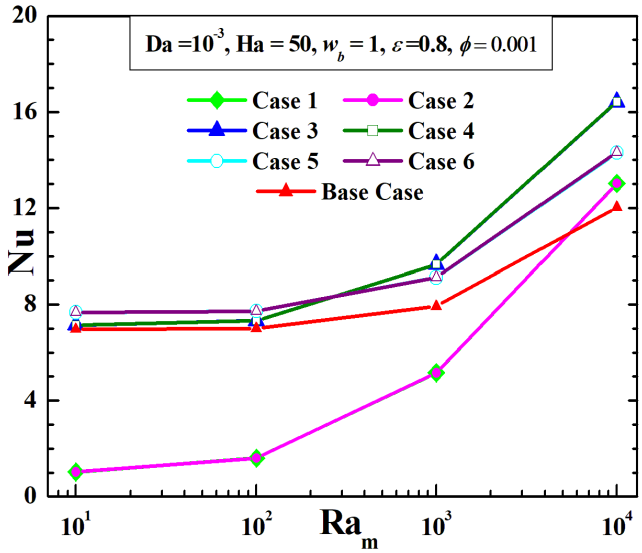

c) Avg Nu vs Ra_m for all heater lengths

Fig. 9: Heat transport curves in terms of Nu local at (a) left source and (b) right source and (c) Nu average for all cases of heater length.

Outside the embedded zone, the streamlines, instead of curving towards the bottom cold wall, proceed to the hot wall. Of course, the sizes of the circulation loops are consistent with the heater sizes. Two small circulation zone are apparent descending downward along the cold walls on either side of the longer heater. Clearly, the circulation within these zones are viscosity driven.

Greater flow connectivity between the middle and top zones can be explained by the natural tendency of the hotter, hence of less denser, fluid to displace the colder fluid on top more easily downward than that in the bottom segment. Consequently, the top zone has a greater proportion of hotter fluid and stronger temperature gradients at its two corners than those near the bottom corners. Hence, the heatlines near the top corners are more aligned with the normal to the isotherms and in rest of cavity dominated more by the convection currents. The swapping of conditions between the two side walls clearly leads to contours that are mirror images about one side wall. Also, the increase in Nu with increase in the heater size arises from the increased heating provided by the heaters. An encouraging feature is the outcome of the MM arrangement as the best over almost the entire Ra_m range with one heater four-time larger than the other.

c) Increased number of heating segments

Effect of number of heating segments of the MM arrangement is explored in Figs. 10 and 11. The height of every segment is chosen identical and values depend on number of segments considered. Persistent augmentation of heating with number of heaters is evident from Fig. 10 at all Ra_m. Clearly, the boundary layers in Fig. 11 are thinner nearer to heating and cooling surfaces along the vertical walls with increase in the number of segments from one to five. Greater transport across thinner boundary layer indeed justifies the predicted increase of Nu with increased segmentation.

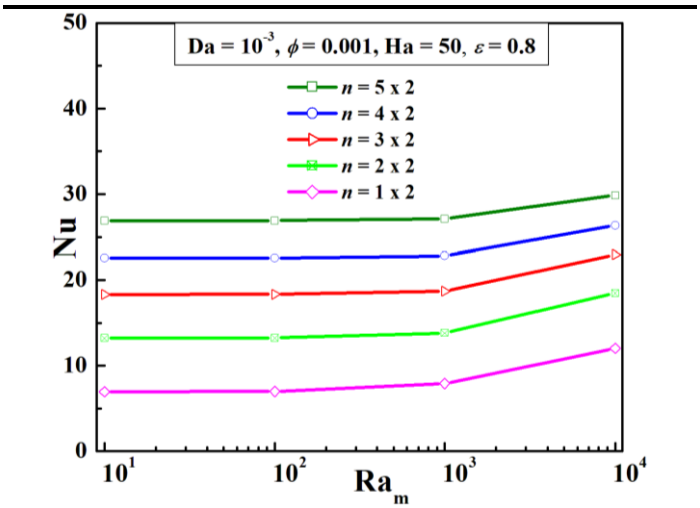

Fig. 10: Heat transfer characteristics in terms of average Nu for heater number change in either side wall.

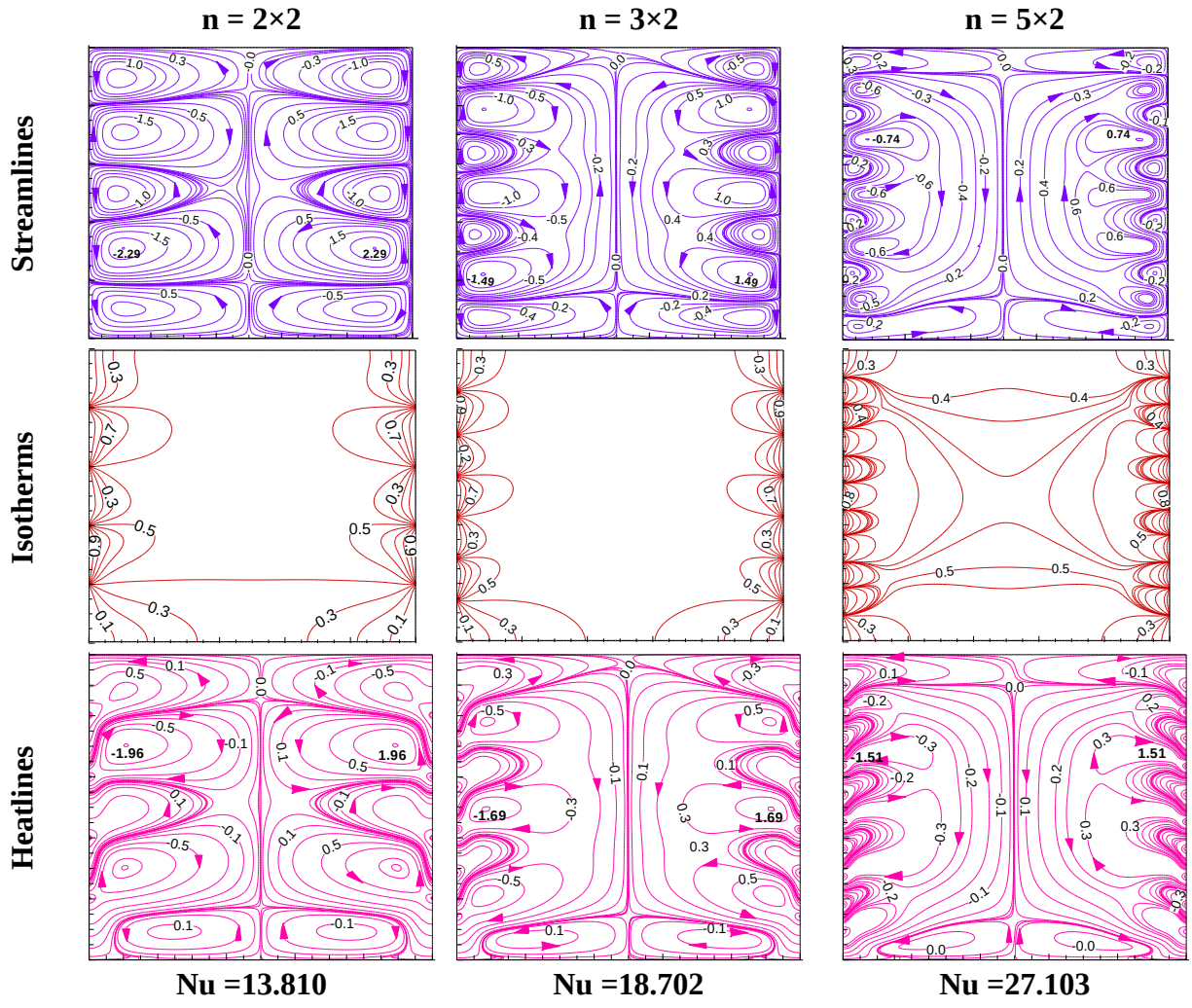

Fig. 11: Thermo-fluid flow-configurations in contours for varying numbers of segmental heater in side walls of an un-tilted square cavity at $Ra_m = 10^3$, Ha = 50, Da = 10^{-3}, ϕ = 0.1%.

d) Different aspect ratios of the cavity

While the MM case of Fig. 5 pertains to a square cavity of height to width ratio, or aspect ratio, AR equal to 1, Figs. 12 and 13 bring out the effect of change of cavity heights by keeping the width same. Two cases of greater heights corresponding to AR of 1.5 and 2.0 exhibit no significant change apart from the expected vertical stretching of the contour patterns. Of course, the functional values differ due to the change in the velocity and temperature gradients for different segment heights. Lower AR implies smaller heater size, hence reduced heating and greater reduction of the horizontal component of velocity towards the vertical plane of symmetry. Despite the greater reduction of the temperature in this zone, the reduced vertical height effectively keeps the convection current set in by the temperature-dependent density gradient along the vertical direction as strong. As a result, the flow from the middle segment exhibits an upwardly rising pattern towards the relatively colder top segment having a denser fluid. This

feature is strikingly evident in case of AR equal to 0.5. No heat transfer across the vertical plane of symmetry makes the heat lines near this plane nearly vertical.

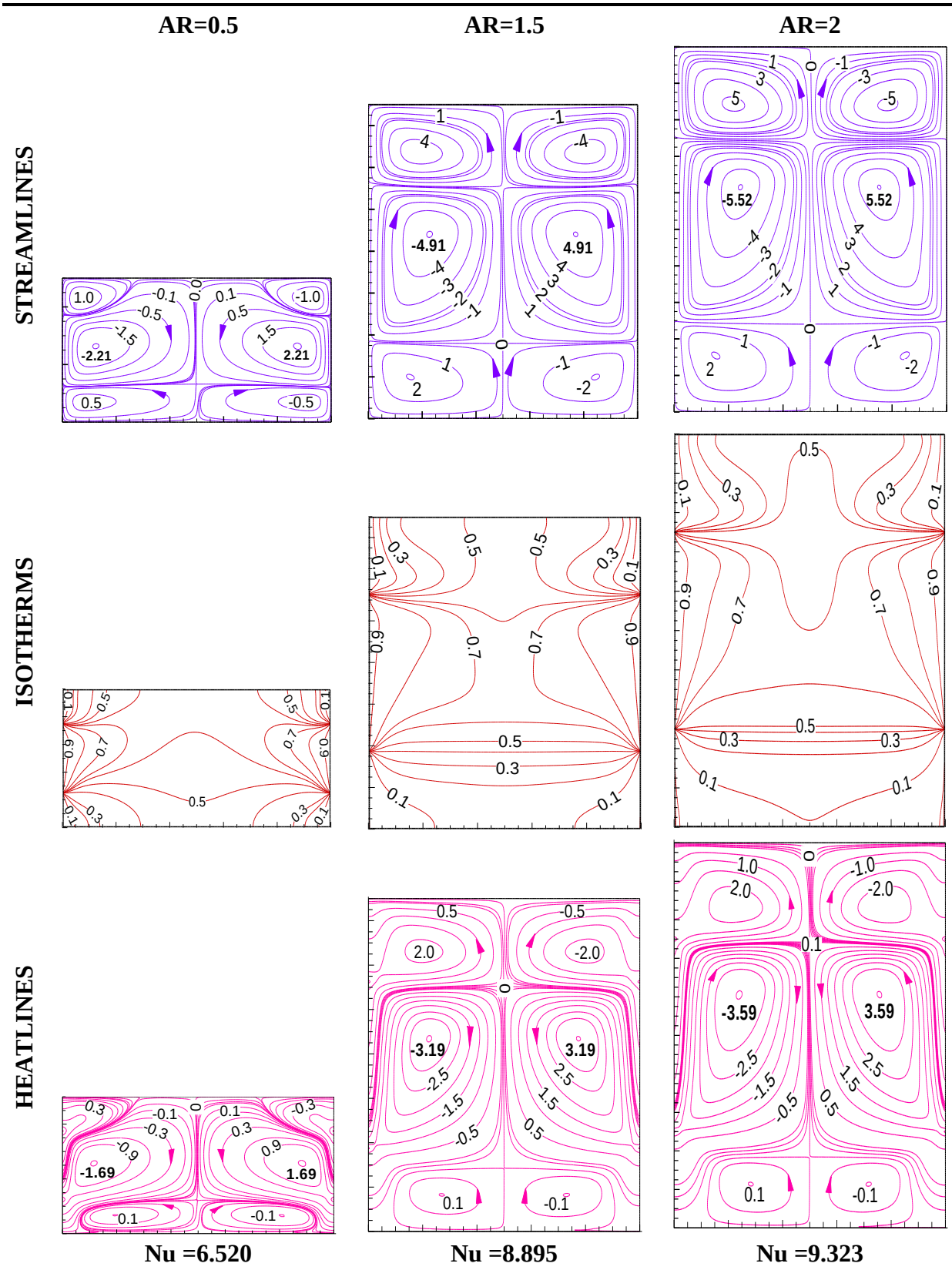

Fig. 12: Variation of thermo-fluid contours for different aspect ratios of the cavity with MM heating at $Ra_m = 10^3$, $Da = 10^{-3}$, Ha = 50, ϕ = 0.1%.

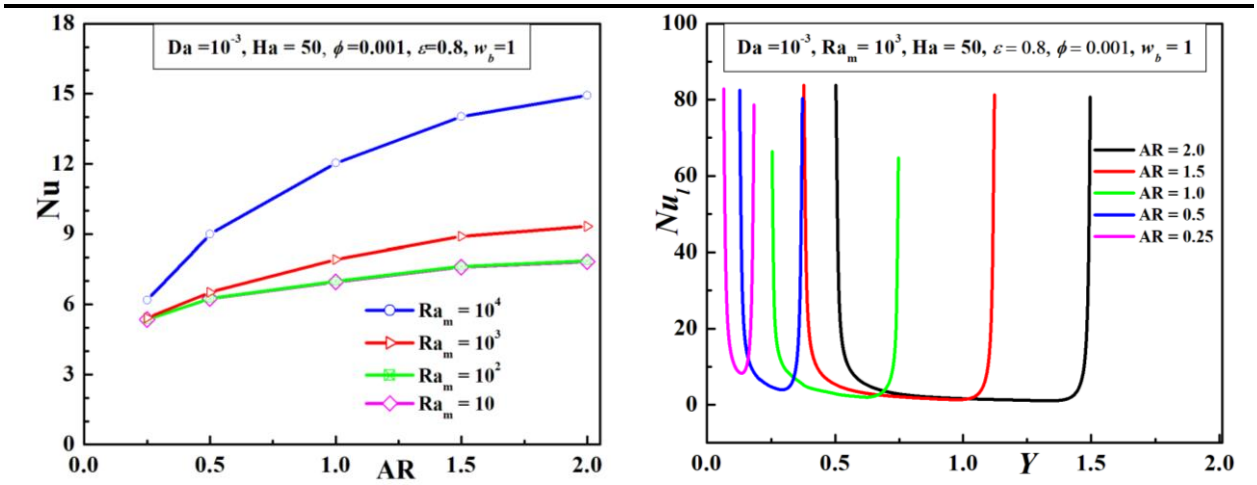

(a) Average Nu (a) Local Nu

Fig. 13: Impact on heat transport characteristics in an un-tilted square cavity in terms of average Nu for different heating arrangements and local Nu with MM heating for different aspect ratios at $Ra_m = 10^3$, Ha = 50, Da = 10^{-3}, ϕ = 0.1%.

The progressive increase in the isotherm values in Fig. 12 from the bottom cold-wall zone up to the top of the hot-wall middle segment and subsequent decrease along the cold-wall zone is consistent with the conduction heat transfer corresponding to the imposed wall temperature condition. Of course, away from the hot wall towards the plane of symmetry, the isotherm values reduce that set in upward convection near the wall in the middle segment due to sidewise drop in temperature and corresponding upward increase in the density. Relatively hotter top segment than the bottom segment is due to the stronger natural convection at the top zone of vertically decreasing temperature and consequently increased fluid density than the viscosity induced flow in the bottom zone with higher density fluid of lower temperature located towards the bottom wall.

The increase in the overall heat transfer at higher aspect ratios evident in Fig. 13 is expected due to greater heating by progressively larger heaters. Of course, the expected increase at higher Ra_m due to convective enhancement is also evident in the figure. Higher spike of the local Nusselt number near the top temperature junction than the bottom one is of course due to the absence of the temperature-driven natural convection in the bottom zone. The variation of the local number in the hot-wall zone between the spikes increases with increase in the aspect ratio in view of the higher vertical gradients of temperature for smaller cavity height for the same cavity width. A notable aspect of the figure is higher spikes with increase in the deviation of the aspect ratio from 1 on its both sides. This can be explained due to the competing events of higher heating and lower temperature gradient with increase in heater and cavity lengths with increase in the aspect ratio. The heating effect seems to dominate with increase of the aspect ratio above 1, whereas the gradient effect appears dominating with decrease in the aspect ratio below 1.

e) Different tilts of the cavity

The effect of different counterclockwise tilts from 0 to 180^o have been captured in Figs. 14 and 15 for $Ra_m = 10^3$, Ha = 50, Da = 10^{-3}, $w_b = 1$, $L_{hl} = L_{hr} = 0.5L$ and $\phi = 0.1\%$. In Fig. 14 pertaining only to the MM arrangement, the tilt of the cavity is not explicitly shown for the brevity of the presentation. The presentation involves an artificial rotation, if necessary, to the nearest un-tilted configuration with one insulated wall visually appearing to be at the bottom. Of course, the insulated walls are identifiable by the near-by heatlines aligned nearly parallel to respective walls.

Since the case of the 180^o tilt involves no artificial rotation, the wall appearing at the bottom and top of the figure are actually the top and bottom walls respectively. This can be concluded from the explanation given in Fig. 12 for the isotherm patterns on either side of the hot-wall middle segment that feeds hot fluid more to the cold segment lying above than the one below as a result of the natural tendency of the hotter fluid to rise above. Corresponding to the equal and opposite artificial rotations employed in the presentation of the 30^o and 150^o cases, the contours in one case appear as flipped of the other case about the line appearing at the bottom. The artificial rotation in the 90^o tilt case shows the vertical adiabatic walls as horizontal and the top and bottom walls with constant-temperature segments as vertical on the right and left sides respectively. In all the arrangements in Fig. 15, the highest Nu arises in the case of 90^o tilt. This is indeed expected in view of the longest vertical separation between the constant high and low-temperature boundaries on opposite walls giving rise to the strongest vertical convection.

Any tilt equally away from 90^0 on either side in the MM arrangement causes interchange of the positions between the rightmost and leftmost walls with constant-temperature segments. Such an interchange does not alter the overall effect, as evident in the symmetric reduction of Nu variation about the 90^o tilt angle. The effects of the interchange is evident also between the TT and BB pairs and the TM and MB pairs. Within each pair Nu is equal at 90^o within numerically acceptable limit and decreases equally for opposite and equal change of the tilt away from 90^o. The vertical walls contain the temperature junction points in the un-tilted and 180^o tilt cases. With approach to 90^o orientation from each, the horizontal distance between the junction and the nearest corner. This causes weakening of the natural convection near the corners for its strongest tendency to be vertical. At any particular tilt, the geometrical arrangements cause the horizontal separation to be the highest for the TT and BB pair and the lowest for MM through TB first and the TM and MB pair next. Such weakening effect is corroborated by the variations of Nu among the different cases. This effect is also evident in the decrease of local heat transfer with decrease in vertical separation between the similar points between the heaters towards the top and bottom sides.

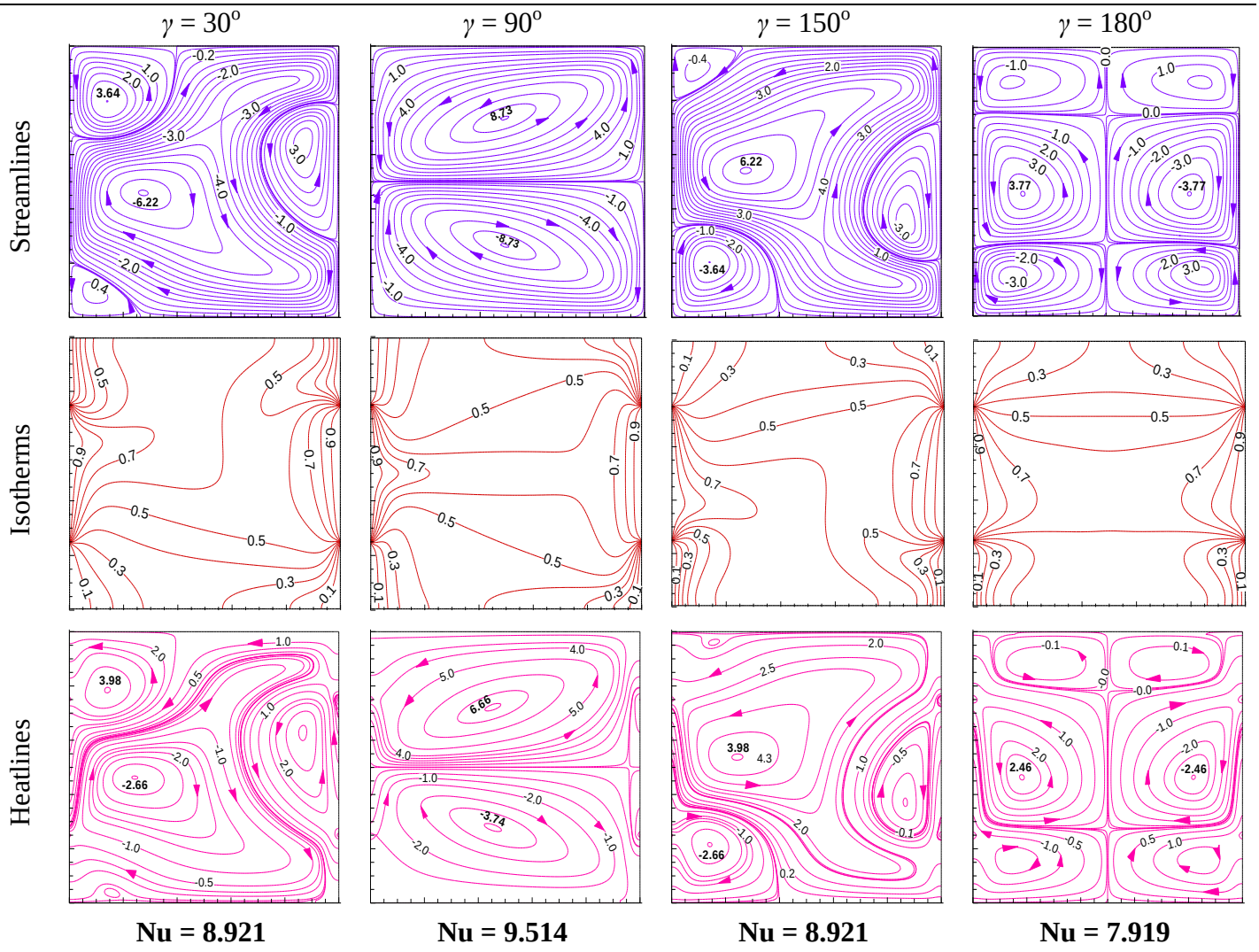

Fig. 14: Variation of thermo-fluid contours for different tilts of the cavity with MM heating at $Ra_m = 10^3$, Ha = 50, ϕ = 0.1%, Da = 10^{-3}.

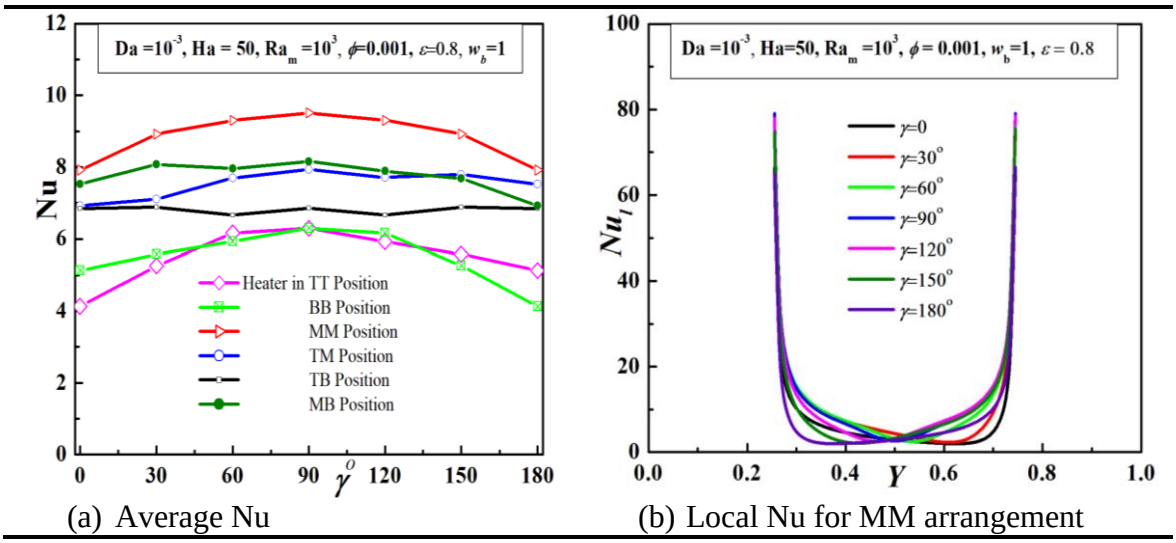

(a) Average Nu (b) Local Nu for MM arrangement

Fig. 15: Impact on heat transport characteristics in an un-tilted square cavity in terms of average Nu for different heating arrangements and local Nu with MM heating for different tilts at $Ra_m = 10^3$, Ha = 50, Da = 10^{-3}, ϕ = 0.1%.

f) Different convection strengths for different Darcy Rayleigh number Ra_m

For un-tilted cavities, Figs. 16 and 17 show the effect of the convection strength that increases with Ra_m with progressive decrease of the damping effect for the same magnetic field. For the MM arrangement in Fig. 16, the increase in the convective strength is evident from the higher value of the maximum stream function at higher Ra_m. The domination of conductive heat transfer is quite clear at Ra_m equal 10 from the orientations of the heatlines chiefly being normal to the isotherms. For Ra_m equal 10^4, significant alignment of the heatlines with the streamlines signifies the domination of the convective flow in heat transfer. The progressive decrease of the flow damping with increase in Ra_m is also apparent in the associated increase in the heat transfer enhancing both Nu and Nu_l by the increase in the convection. As explained in the context of Fig. 7, increased heat transfer at higher Ra_m and for greater vertical separation between the hottest and the coldest segments captured in Fig. 17 presumably arises from developing flow instabilities.

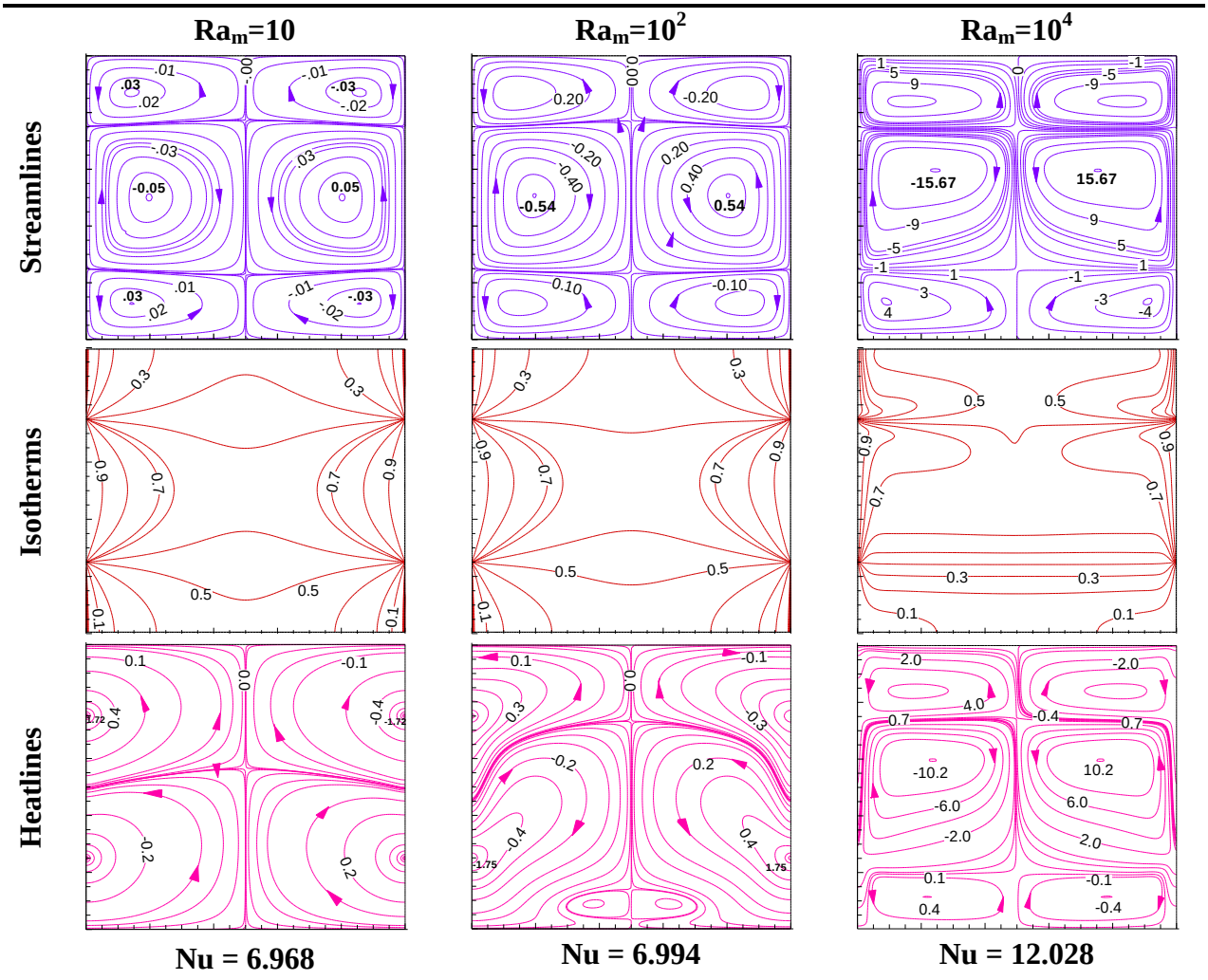

Fig. 16: Variation of thermo-fluid contours for different Darcy-Rayleigh numbers with MM heating at Ha = 50, Da = 10^{-3}, ϕ = 0.1%.

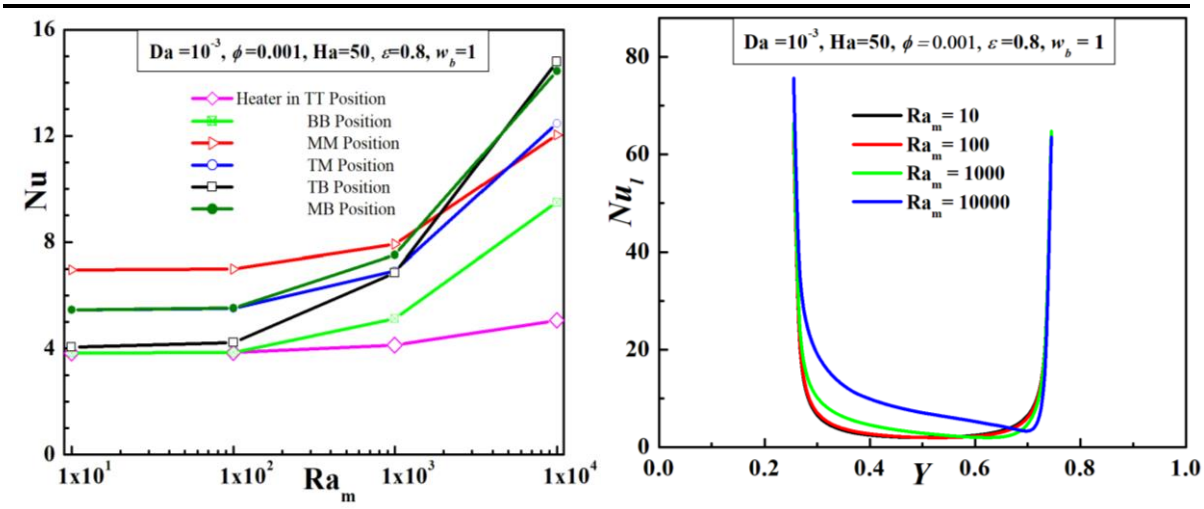

(a) Average Nu (b) Local Nu for MM arrangement

Fig. 17: Impact on heat transport characteristics in an un-tilted square cavity in terms of average Nu for different heating arrangements and local Nu with MM heating for different convection strengths of at Ha = 50, Da = 10^{-3}, ϕ = 0.1%.

g) Different permeability of porous cavity for different Da

The effect of different permeability of the porous cavities captured by different Da under constant Darcy-Raleigh number Ra_m are shown in Figs. 18 and 19. It may be noted that Ra_m is the product of Raleigh number Ra and Da. Higher Ra signifies higher natural or free convective strength induced by the density variation in an inverse manner with temperature in the flow that takes place through the pores of the porous medium. On the other hand, higher Da approaching 1 in a cavity without any porous structure inside implies lower fraction of the cavity occupied by the porous medium. Hence, higher Da leads to lower convection due to increase in the resistance to the flow offered by the reduced extent of the porous wall. But, increase in Da at constant Ra_m means a simultaneous decrease of Ra. Of course, a decrease of Ra for constant Da brings down the strength of the thermally-induced convection. Hence, the increase of Da at constant Ra_m is confronted by two opposite effects. One is of increased convection due to increase in permeability with decrease in volume of the porous structure. The other is decreased convection due to decrease in the thermally-induced convection.

From the decreases in average Nu values for the three case in Fig. 18 and the average and local variations of Nu in Fig. 19 with increase of Da at constant Ra_m, the domination of the effect of lower Ra over higher Da is evident. Similar domination is also apparent in the stream line contours in case of the lowest Da. This is revealed by highest and lowest function values for the similarly-located streamlines for the lowest and the highest Da cases and closer alignment of the heatlines with the streamlines over most of the cavity in the lowest Da case.

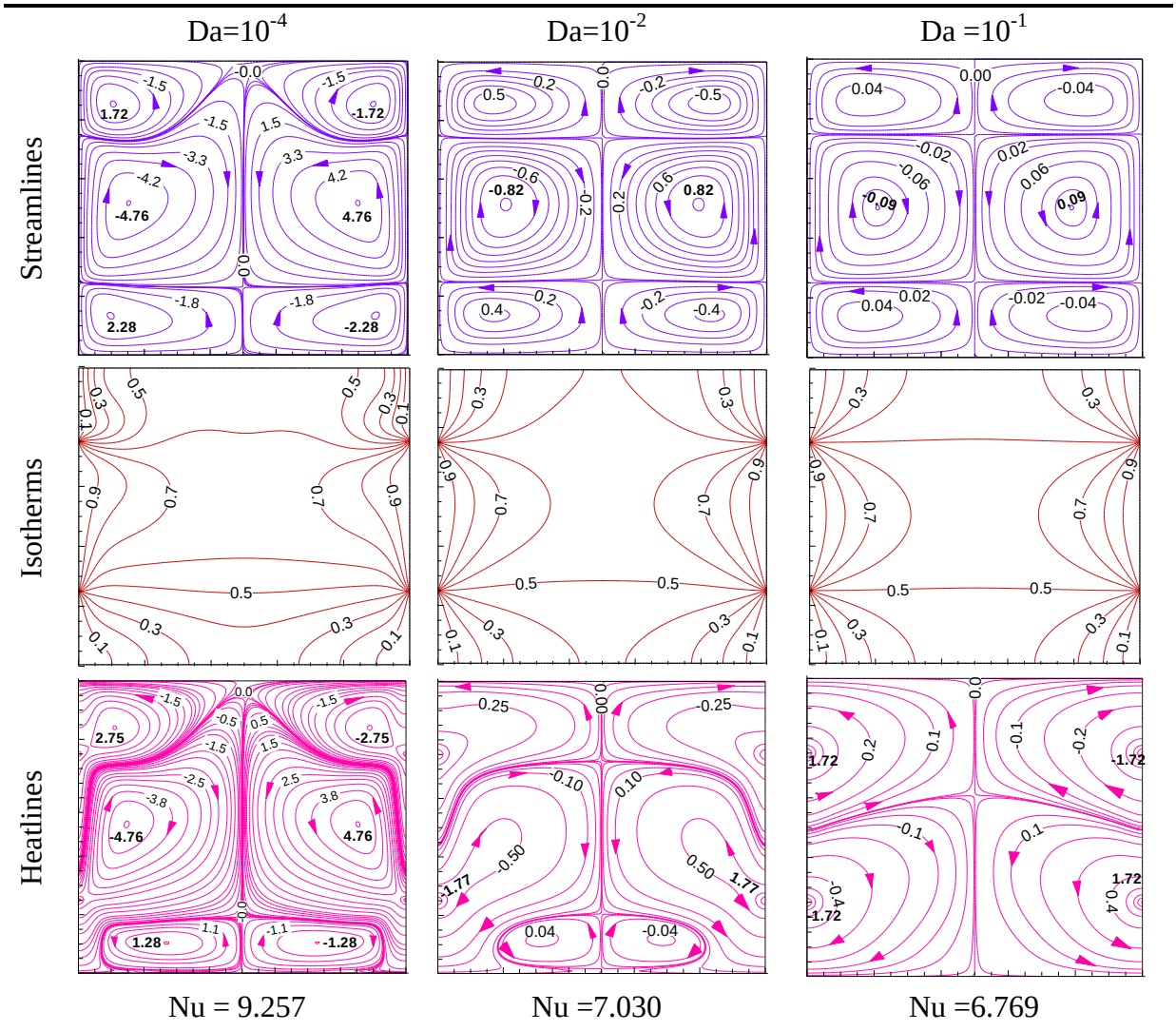

Fig. 18. Variation of thermo-fluid contours for different Darcy numbers with MM heating in a square cavity at $Ra_m = 10^3$, Ha = 50, ϕ = 0.1%.

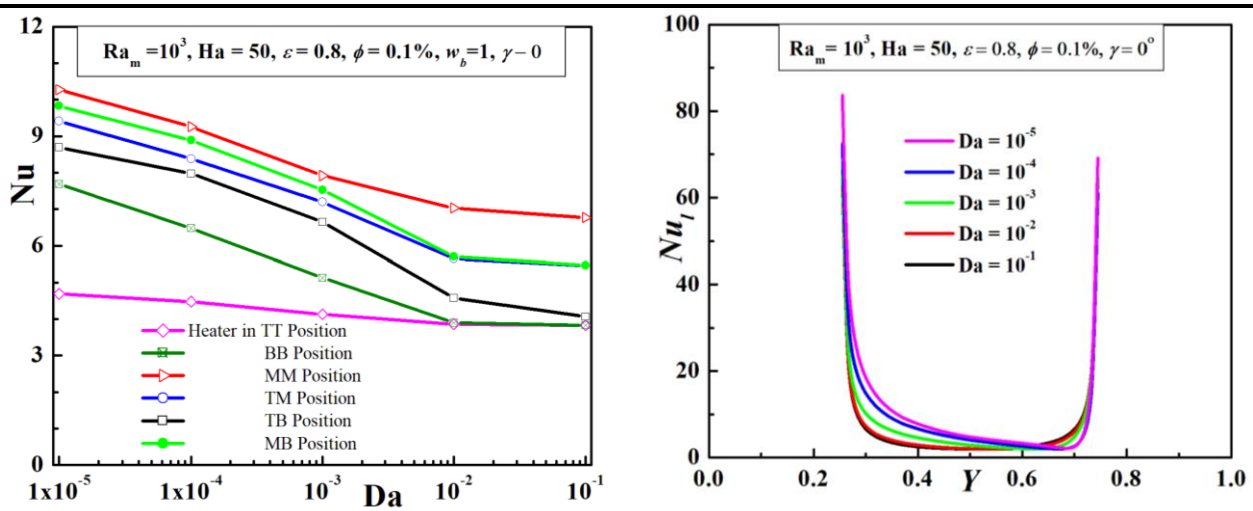

(a) Average Nu (b) Local Nu for MM arrangement

Fig. 19: Impact on heat transport in an un-tilted square cavity in terms of average Nu for different heating arrangements and local Nu with MM heating for different Darcy numbers at $Ra_m = 10^3$, Ha = 50, ϕ = 0.1%.

h) Different porosity index ε of cavity

Higher porosity index ε of the cavity implies greater capacity of the porous material within the cavity to retain fluid within it. As a result of the higher retention, the flowing fluid volume gets effectively reduced. Hence, the strength of the thermally-induced convection current becomes higher. In other words, the effect of increase of ε is expected to be similar to the increase in Darcy Rayleigh number Ra_m discussed earlier. The effects of different ε are presented in Figs. 20 and 21.

Higher convective flow at higher ε is evident in Fig. 21 from the higher function values of the similarly located streamlines especially in the top and middle segments. Across the hot-wall middle segment, the natural tendency of hot fluid to ascend and cold fluid to descend makes the top and bottom segments progressively hotter and colder. Relatively higher amount of hotter fluid in the top segment and colder fluid in the bottom segment is evident from the isotherm contours. This can be inferred from the expansion of the hottest zones between the higher isotherm values of 0.5 and 0.6 in the top segment than between 0.3 and 0.5 in the bottom segment.

The heatline contours reveal the domination of the convection except near the corners in all the cases studied. In contrast to Fig.15 exhibiting larger extent of the domination of conduction predicted at low Ra_m of 10, no such region has arisen in Fig. 21. Also, the instability-driven high rate of rise of heat transfer values apparent in Fig. 16 beyond a certain Ra_m does not arise for any ε in Fig. 20 since this index is not related to such physical mechanism of augmentation. In absence of the possibility of setting of instabilities with change in ε, variation with it for both the average and local Nusselt number in any particular heating arrangement indeed appears to be low. However, the different heating arrangements lead to variations over different short ranges.

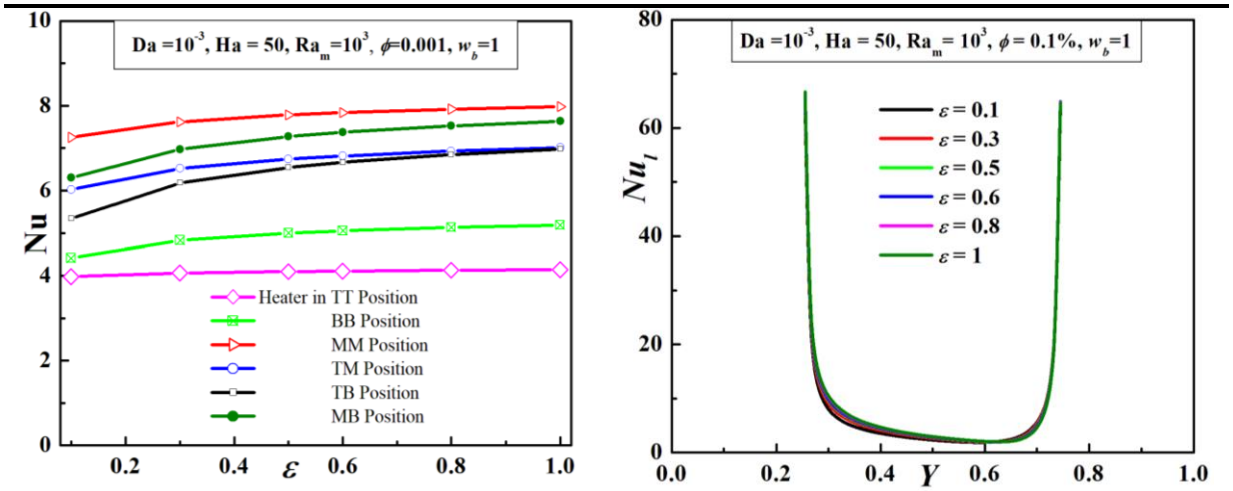

(a) Average Nu (b) Local Nu for MM arrangement

Fig. 20: Impact on heat transport in an un-tilted square cavity in terms of average Nu for different heating arrangements and local Nu with MM heating for different values of porosity index at $Ra_m = 10^3$, Ha = 50, ϕ = 0.1%, Da = 10^{-3}.

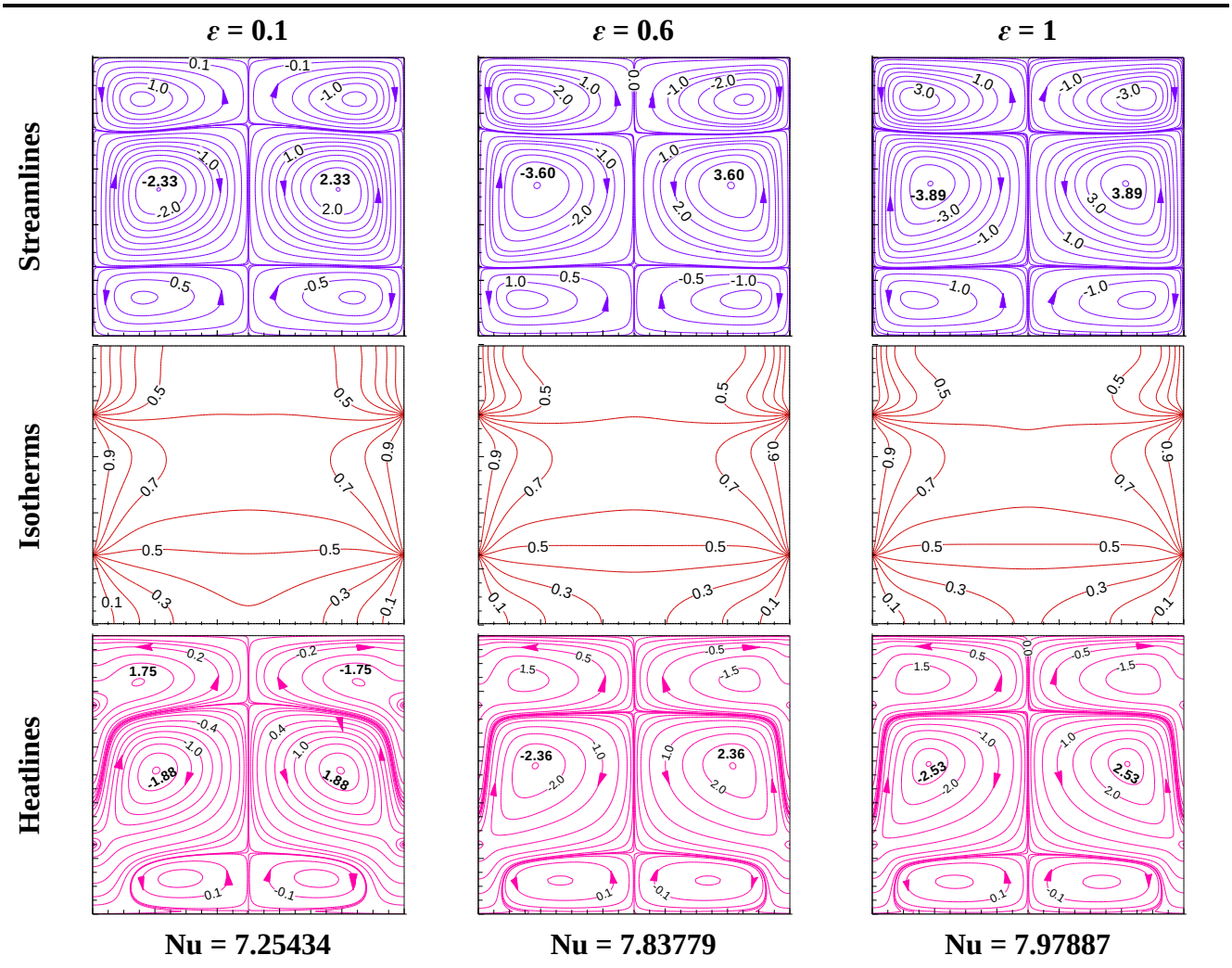

Fig. 21: Variation of thermo-fluid contours for different values of porosity index with MM heating at Ha = 50, Da = 10^{-3}, ϕ = 0.1% at $Ra_m = 10^3$, Ha = 50, ϕ = 0.1%, Da = 10^{-3}.

i) Different nanoparticle volume fractions

In Figs. 22 and 23, the effect of addition of nanoparticles to the base fluid at increasing proportion are presented. The decrease in the similarly located stream function values in Fig. 22 reveal the expected decrease of the strength of the convection with increase in the higher-density particle volume. However, the isotherm and heatline contours appear to be little affected by the change due to the compensation against the reduced convection provided by the higher thermal conductivity of the particles than the fluid. The Nu value in this figure shows marginal increase with increase in the volume fraction indicating marginal enhancement of the heat transfer. Of course, the strength of the convective flow are different for different heater arrangements that is evident from the nature of variations of the average and local Nusselt numbers in each case in Fig. 23. Though in a minor way, the addition of nanoparticles augments heat transfer in the MM case from the highest Nu values among the different cases considered in the figure.

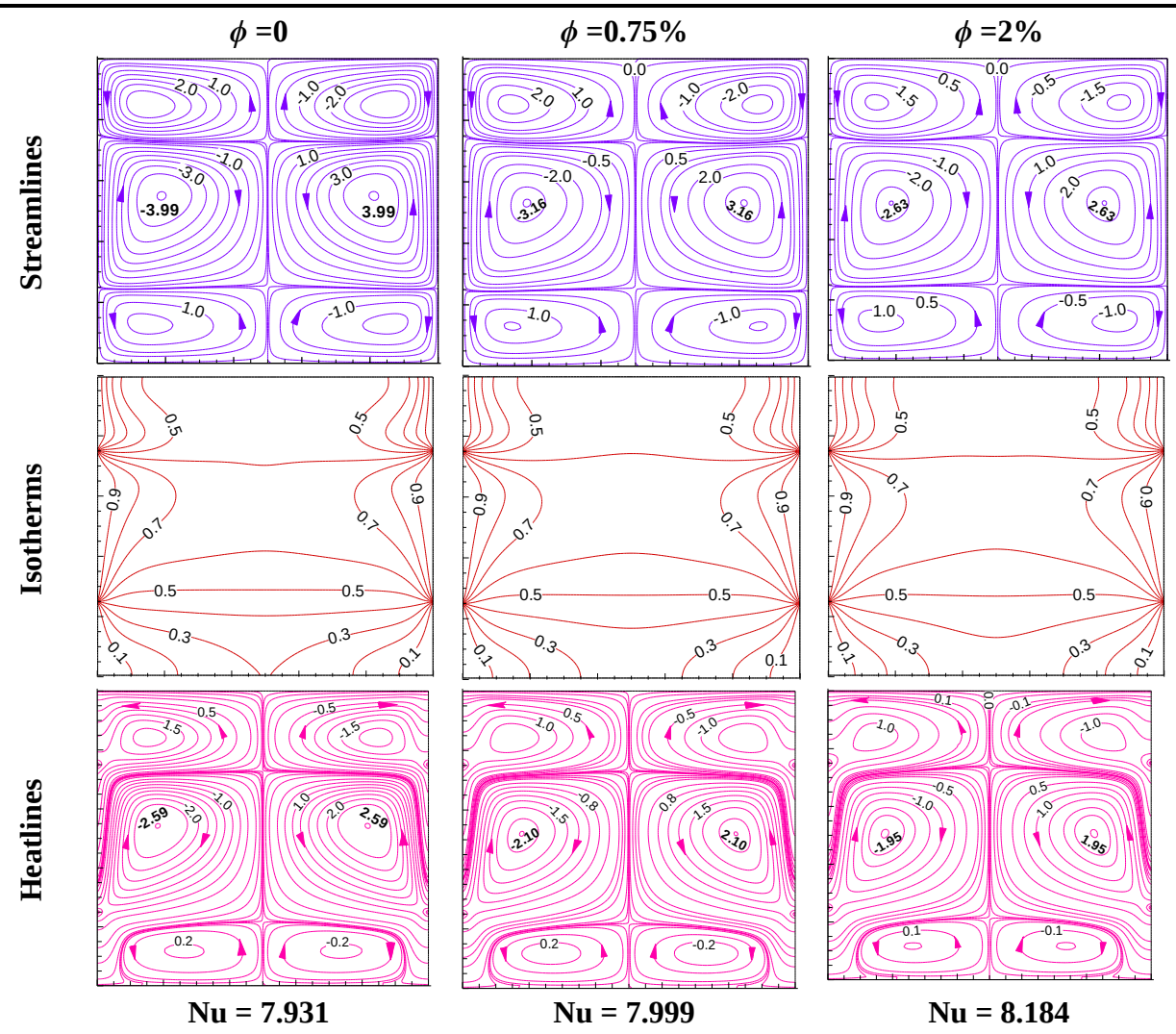

Fig. 22: Variation of thermo-fluid contours for different nanoparticle volumes with MM heating in a square cavity at $Ra_m = 10^3$, Ha = 50, $Da = 10^{-3}$.

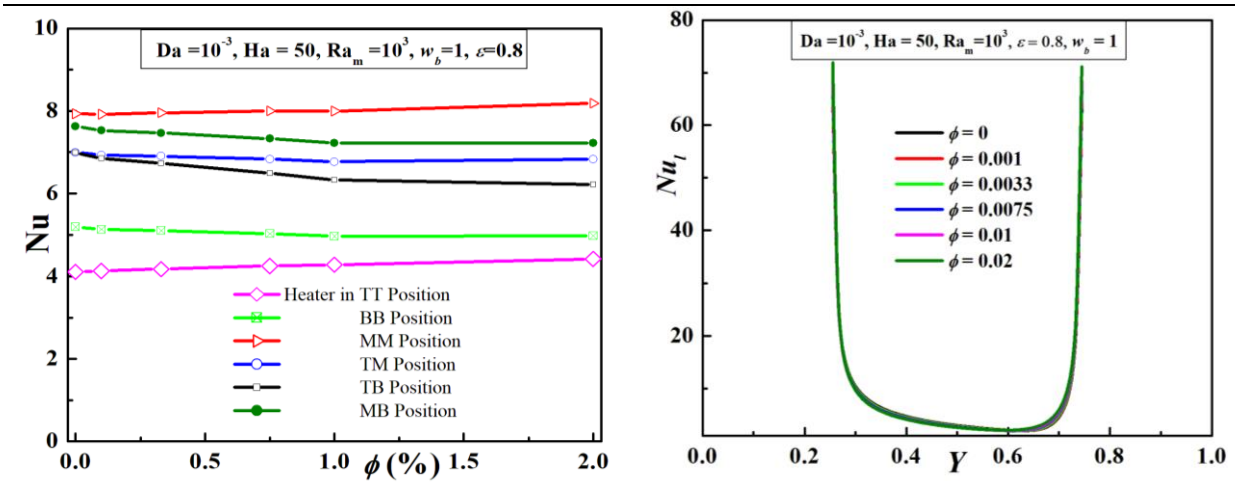

(a) Average Nu (b) Local Nu for MM arrangement

Fig. 23: Impact on heat transport in an un-tilted square cavity in terms of average Nu for different heating arrangements and local Nu with MM heating for different nanoparticle volumes at $Ra_m = 10^3$, Ha = 50, $Da = 10^{-3}$.

Part 2: Magnetic fields of different strengths, angles and segmental variations

a) Effect of magnetic field intensity for different Hartmann numbers

The effect the variation of Hartmann number Ha for a horizontal whole-domain magnetic field imposed uniformly are shown in Figs. 24 and 25. In Fig. 24, the decrease in the highest stream function value with increase in Ha can be attributed to the increased flow damping. But, higher damping is known to cause increased heating. Nearly similar isothermal patterns implies the reduced heat transfer due to decreased convection to get compensated by the damping-related heating. For each heater arrangement, this is evident also in Fig. 25 from the predicted short-range variation of the average and local Nu with Ha. Except near the corners, the heatline contours in Fig. 24 appear to be dominated by the convective effect over the conduction effect.

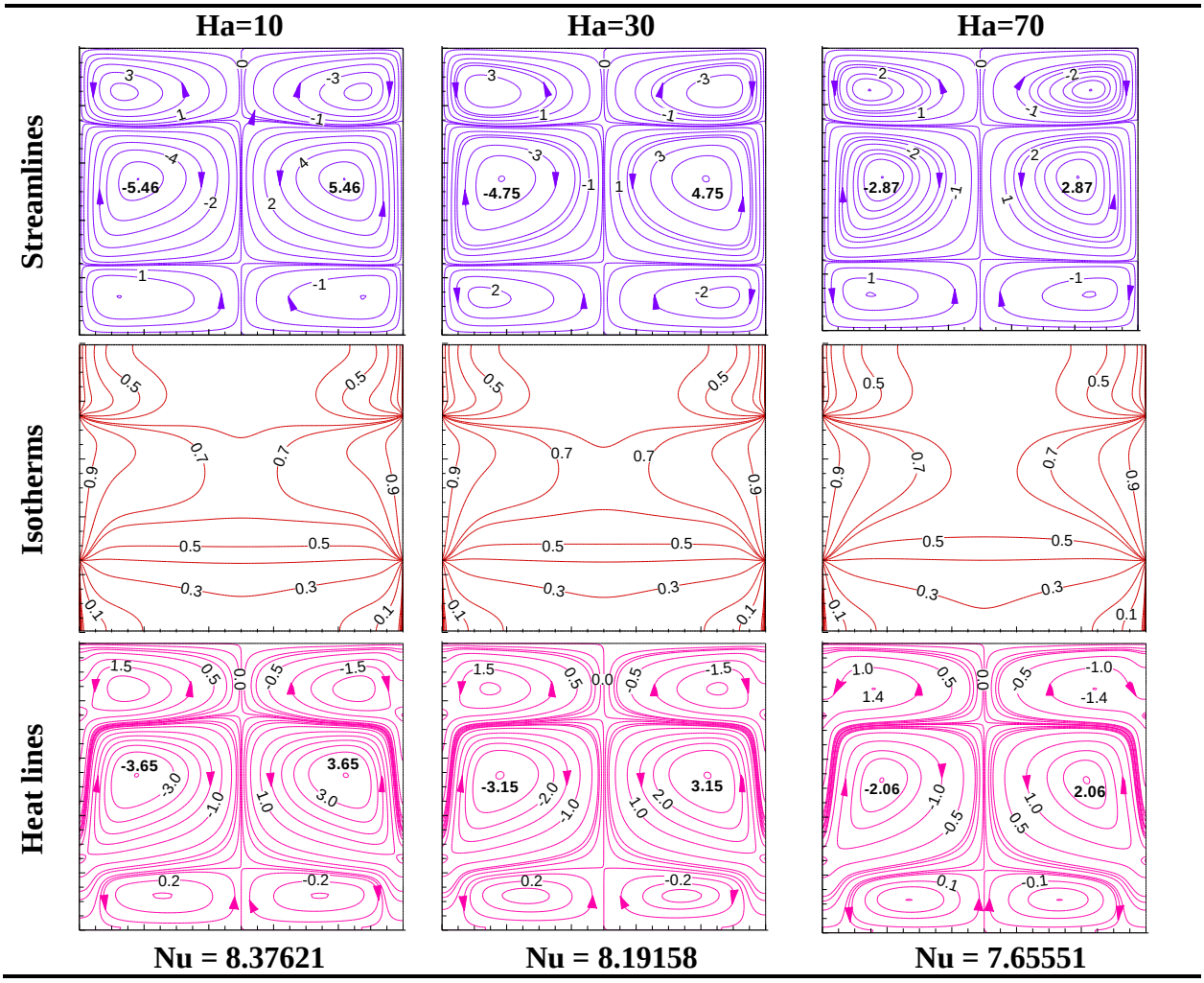

Fig. 24: Variation of thermo-fluid contours with MM heating in an un-tilted square cavity for different whole-domain Ha at $Ra_m = 10^3$, $\phi = 0.1\%$, $Da = 10^{-3}$.

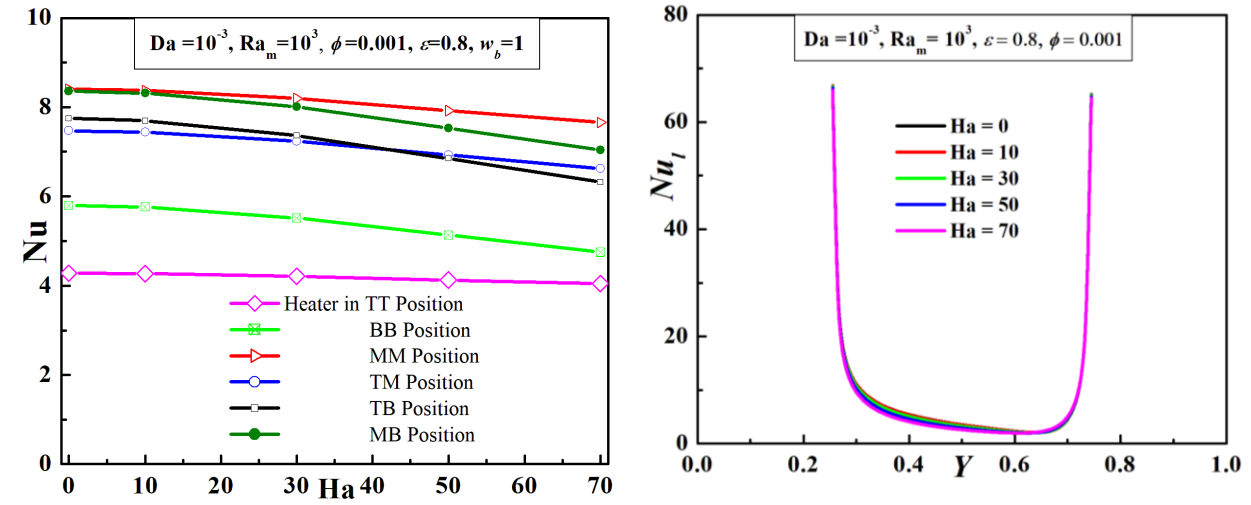

(a) Average Nu **(b) Local Nu for MM arrangement**

Fig. 25: Impact on heat transport in an un-tilted square cavity in terms of average Nu for different heating arrangements and local Nu with MM heating for different whole-domain Ha at $Ra_m = 10^3$, $\phi = 0.1\%$, $Da = 10^{-3}$.

b) Effect of magnetic field angle (β)

The effect of counterclockwise variation of the field angle β of the whole-domain magnetic field over the range 0 to 180^o is shown in Figs. 26 and 27. Of course, the symmetry of the heating arrangement about the vertical mid-plane for the TT, MM and BB arrangements keeps all the variations for the field angles 0, 90^o and 180^o symmetric. For the in-between angles, the contours develop asymmetry that is expected to be the maximum at about β equal to 45^o and 135^0 lying midway between the two symmetric distributions.

The expected flipping about the vertical mid plane of the asymmetric contour lines for equal change of β about the 90^o case is captured in Fig. 26 for the 45^o and 135^o cases under the MM heating arrangement. This is consistent with the symmetric variation about for the average Nu for this case as well as the TT and BB cases in Fig. 27. The attainment of the maximum average Nu at 45^o and 135^o that is quite evident in case of the BB arrangement may be linked with maximum contour asymmetries expected around that location. Among the noted Nu values in Fig. 26, the maximum arises for these two angles in the MM case. But in Fig. 27, the maximum is not so apparent for its closeness with respect to the near-by values corresponding to the symmetric contour cases of 0, 90^o and 180^o field angles. The local Nu variations for the MM case presented in Fig. 27 indeed reveals not very significant effect induced by the angular variation of the applied magnetic field, The symmetric variation of Nu about the 90^o angle for the TM, TB and MB cases, is not expected for not having the geometric symmetry in these heating arrangements. This asymmetry is quite prominent in the variation of the average Nu in Fig. 27 for the MB case.

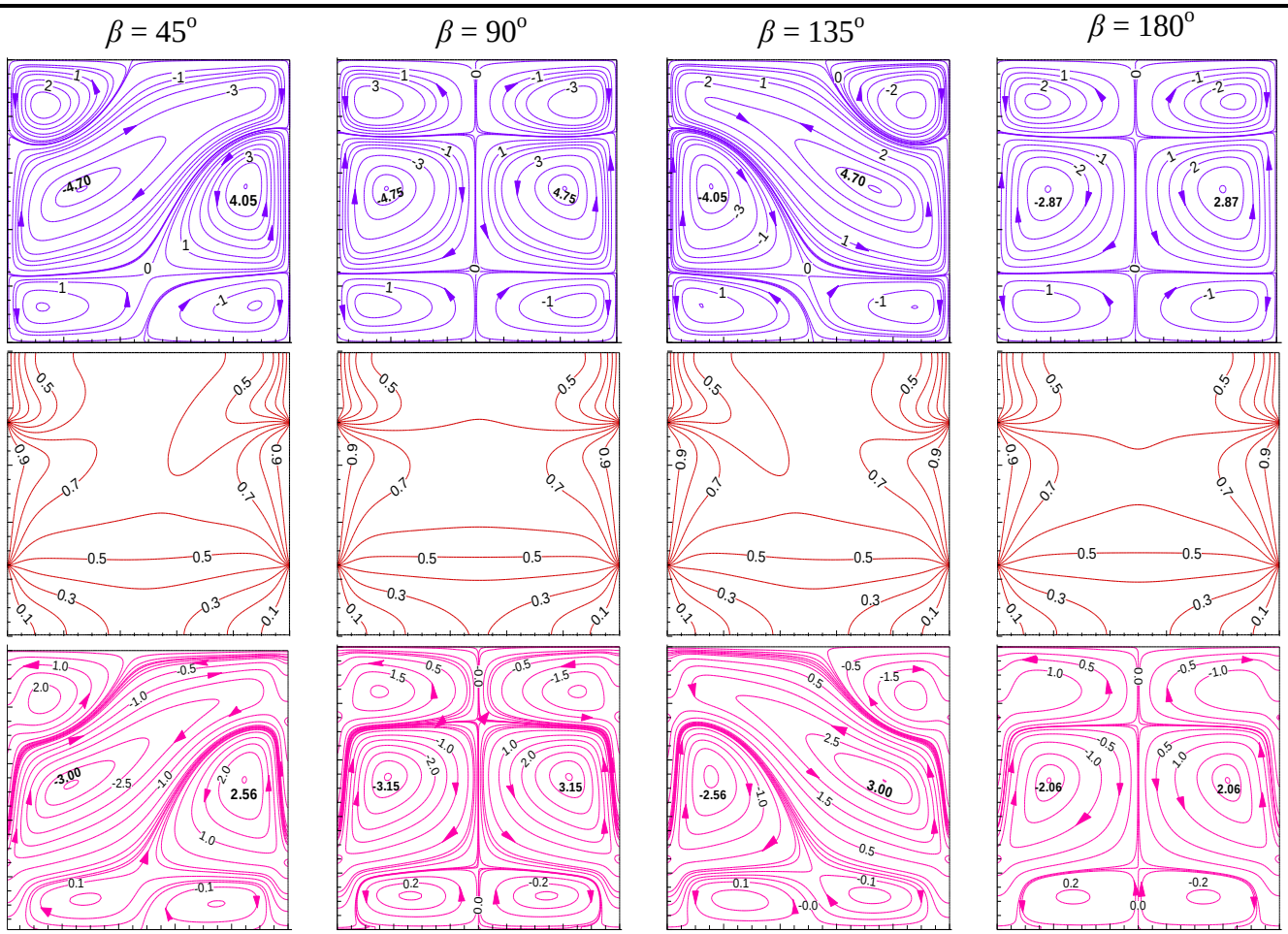

Fig. 26: Variation of thermo-fluid contours with MM heating in a square cavity for different whole-domain magnetic field angles at $Ra_m = 10^3$, Ha = 50, $Da = 10^{-3}$, ϕ = 0.1%.

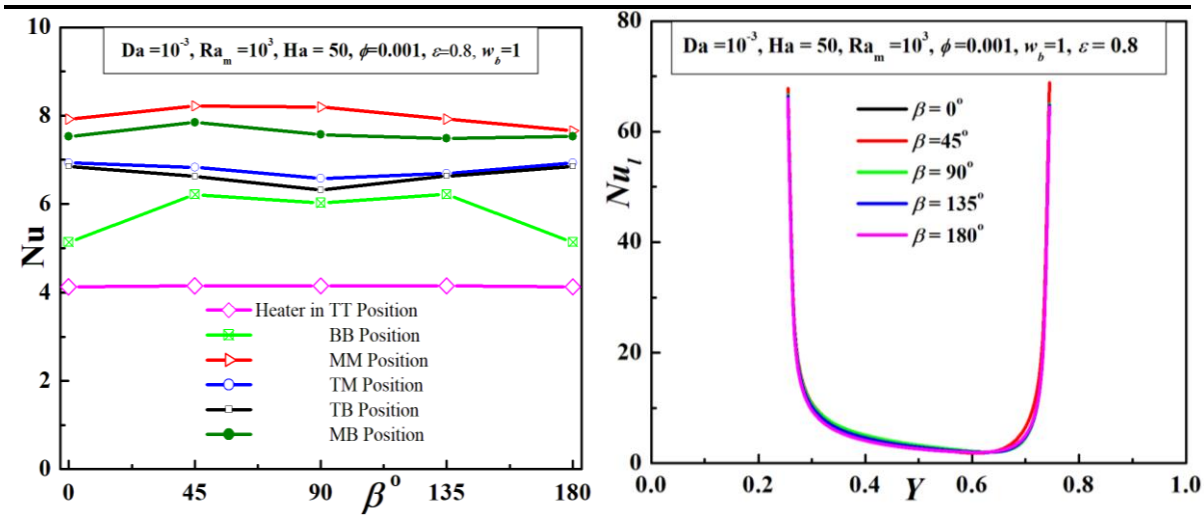

(a) Average Nu (b) Local Nu for MM arrangement

Fig. 27: Impact on heat transport in an un-tilted square cavity in terms of average Nu for different heating arrangements and local Nu with MM heating for different whole-domain magnetic field angles at $Ra_m = 10^3$, Ha = 50, $Da = 10^{-3}$, ϕ = 0.1%.

c) Effect of segment width

Progressively increased damping effect on the flow expected with increase in the centered segment width w_b of horizontal magnetic field in an un-tilted square cavity is evident in Fig. 28 for the MM heating arrangement from the reduction of the highest stream function. However, the effect on the isotherm and heatline contours and the average Nu appear as only marginal in this figure along with the local variation of Nu given in Fig. 29. For the other types of heating arrangements, similarly weak effect on the average Nu is apparent in the figure.

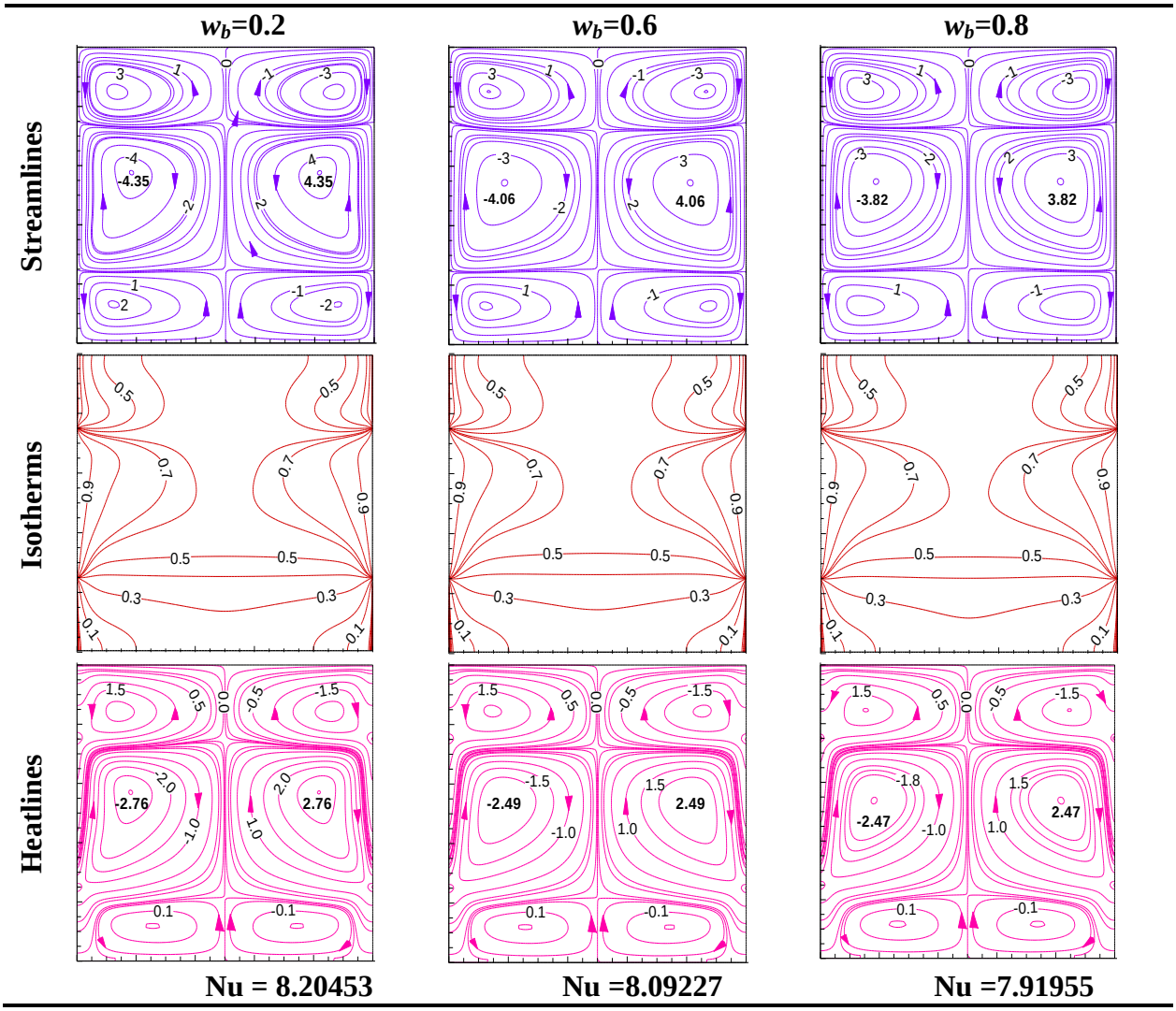

Fig. 28: Variation of thermo-fluid contours with MM heating in an un-tilted square cavity for different segment widths of centered horizontal magnetic field at Ha = 50, Da = 10^{-3}, Ra_m = 10^3, ϕ = 0.1%.

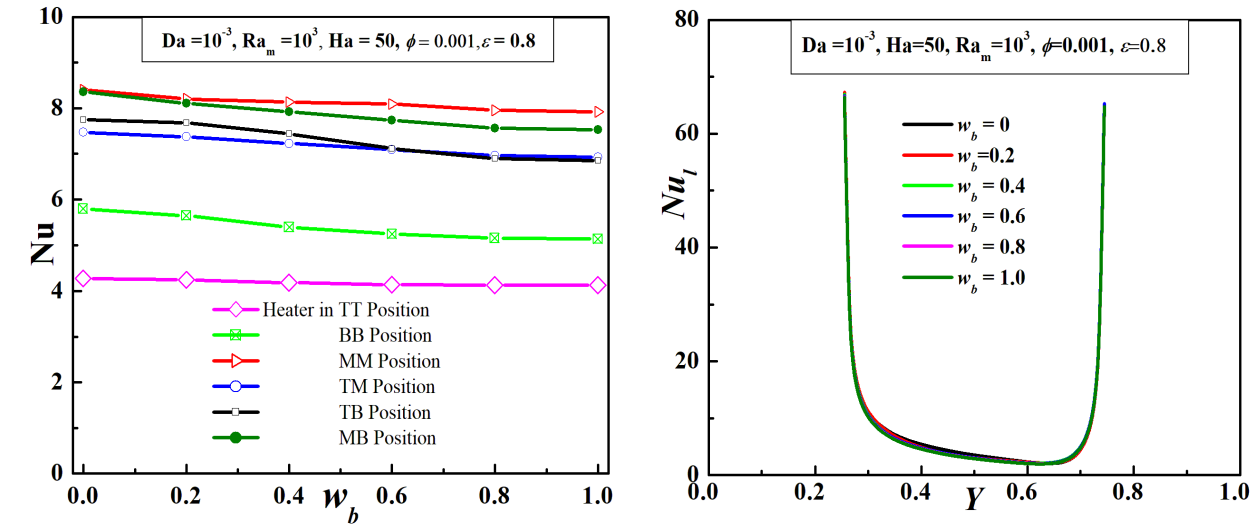

(a) Average Nu **(b) Local Nu for MM arrangement**

Fig. 29: Impact on heat transport in an un-tilted square cavity in terms of average Nu for different heating arrangements and local Nu with MM heating for different segment widths of centered horizontal magnetic field at Ha = 50, Da = 10^{-3}, $Ra_m = 10^3$, ϕ = 0.1%.

d) Effect of positioning of constant-width magnetic segment for different cavity tilts

The effect of positioning of a horizontal magnetic segment of width w_b equal to 0.4 in a square cavity is examined in Fig. 30 for an un-tilted cavity with MM heating of 0.5 size. The lowest maximum stream function value arises in the strongest-flow middle thermal segment. This is indeed due to the higher magnetic damping for the full containment of the centered magnetic segment than having only part overlap extended from either top or bottom magnetic segment.

In the cases of top and bottom magnetic segment, the increased heating due to the higher magnetic damping of the flow reduces the temperature gradient near the respective junction point. With respect to the MM case, the strength of the convective current in each case reduces together with reduction of the viscosity due to higher temperature at the respective interface of the thermal segments. The combined effect is reduced energy draining from the middle thermal segment by the viscous action to the adjacent thermal segment to the top or bottom. Of course, the bottom thermal segment has higher proportion of high-density mass than the top segment at relatively higher temperature imparted by the natural tendency of liquid to rise along a hot wall to a cold wall. Hence, the weakening of the energy draining is more severe in case of the top magnetic segment than the case with bottom one. This explains the lower maximum value of the stream function value in the middle thermal segment under partial coverage by the top magnetic field than by the other case of overlap with the bottom magnetic field. The associated lower enhancement in heat transfer in the average Nu from centered magnetic-field case arises in the former case.

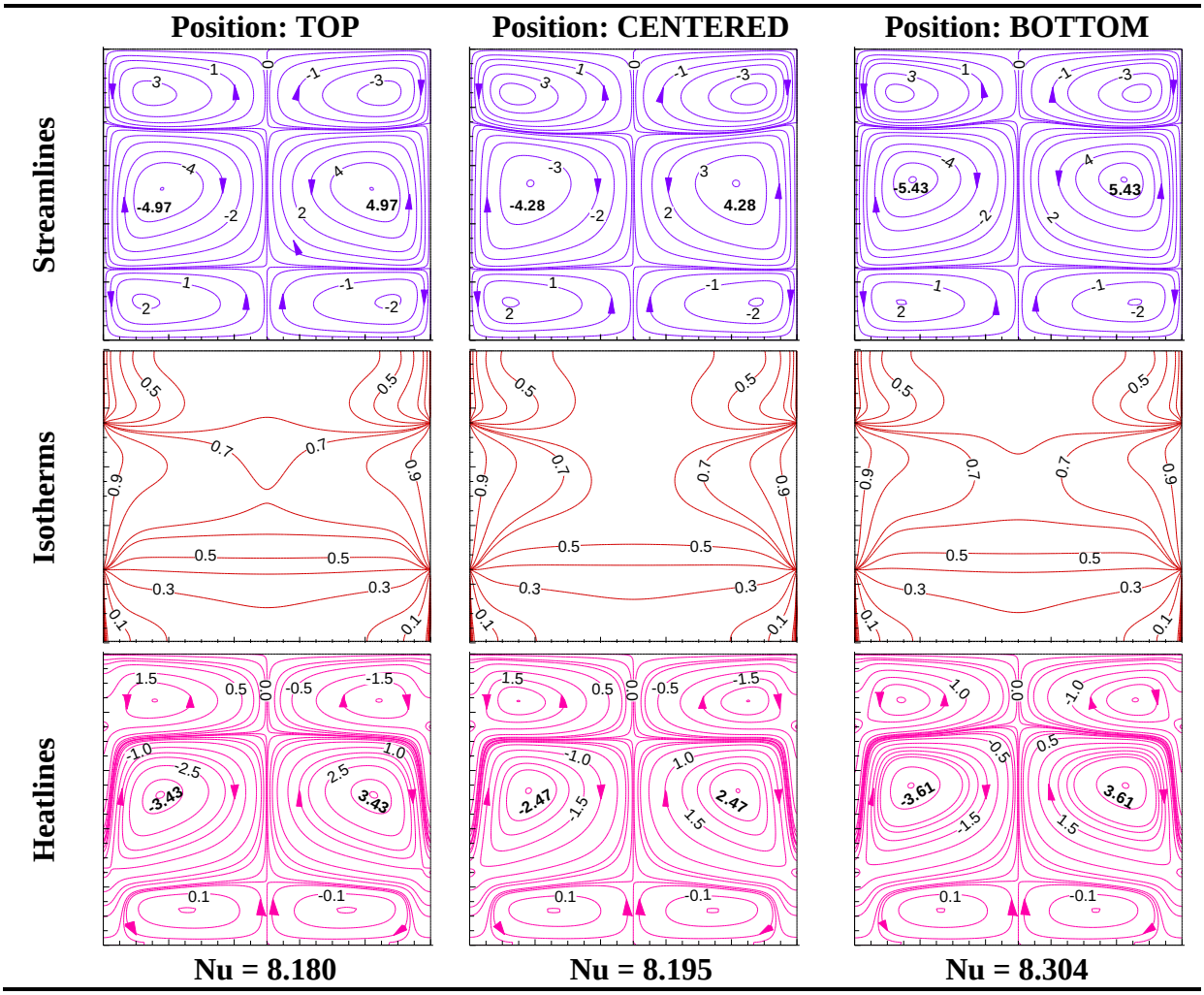

Fig. 30: Variation of thermo-fluid contours with MM heating in an un-tilted square cavity for different positions of horizontal magnetic segment at Ha = 50, Da = 10^{-3}, Ra_m = 10^3, ϕ = 0.1%, w_b = 0.4.

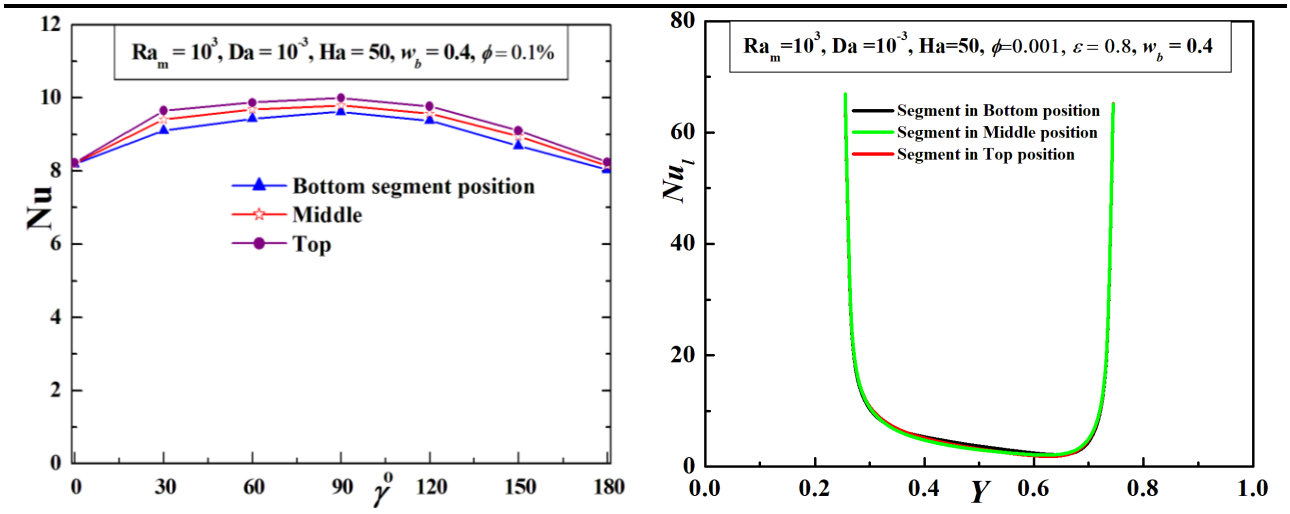

Fig. 31: Impact on heat transport in a square cavity with MM heating under magnetic segment in terms of average Nu for different cavity tilts and local Nu for un-tilted cavity with Ha = 50, Da = 10^{-3}, Ra_m = 10^3, ϕ = 0.1%, w_b = 0.4.

In Fig. 31, the effect tilting of the cavity significantly alters the interaction between the convection set by the temperature gradient in the vertical direction especially in the middle thermal segment. In case of the 90^o tilt, each segment interface is vertical with largest horizontal separation from the wall. Of course, the strongest retarding effect of the boundary layer arises in the 0 and 180^o tilt cases for having the temperature junction points on the vertical walls. Also, the vertical temperature gradient set in this case by the temperature gradient across the wall is clearly lower than that across the vertical line through the temperature junction points on the horizontal wall for the 90^o tilt case. However, the progressive weakening effect of the magnetic damping with the change of tilt on either side of the 90^o case is the strongest in case of the centered magnetic segmenting positioned mostly away from any wall. For the top and bottom magnetic segmenting, the magnetically damped flow region always has a strong overlap with one wall boundary layer. These competitive effects of setting of the strongest current and strongest weakening by magnetic damping along with increased proportion of heavier fluid always towards the bottom justifies the predicted variation of the average Nu in Fig. 31. However, their variations lie in a closed band, reflected also in the variations of the local Nu.

e) Effect of different number of magnetic segments

The study presented in Figs 32 and 33 pertains to multiple segmentation of horizontal magnetic field of total width w_b equal to 0.4 in an un-tilted square cavity. In all the cases beyond the case of single central segment, the widths of the segment and the gaps have been taken as equal to each other located by maintaining symmetry about the horizontal mid plane. In case of MM heating, Fig. 32 reveals marginal decrease in the thermally induced convection strength consistent with the findings and explanation of increased magnetic damping effect on the flow provided in case of Fig. 24 with whole-domain application. A similar compensation to reduced heating from the decrease of convection strength by the increased heating due to the magnetic damping is apparent in both the cases from the insignificant effects on the isotherm and heatline contours in the respective cases. Irrespective of the type of the heating arrangement, the variation of the average Nu in Fig. 33 shows little perceptible change from increase of number of segments beyond 2. Of course, this is an important finding from the application viewpoint. It would also be interesting to study, whether a ferro-fluid would provide higher effect of application of the magnetic field and its segmentation. In case MM thermal segmentation, the variation of the local Nu in Fig. 33 for the cases of different magnetic segmentation also show little differences. In the next chapter, an overall conclusion is drawn and the scope of possible future studies are identified.

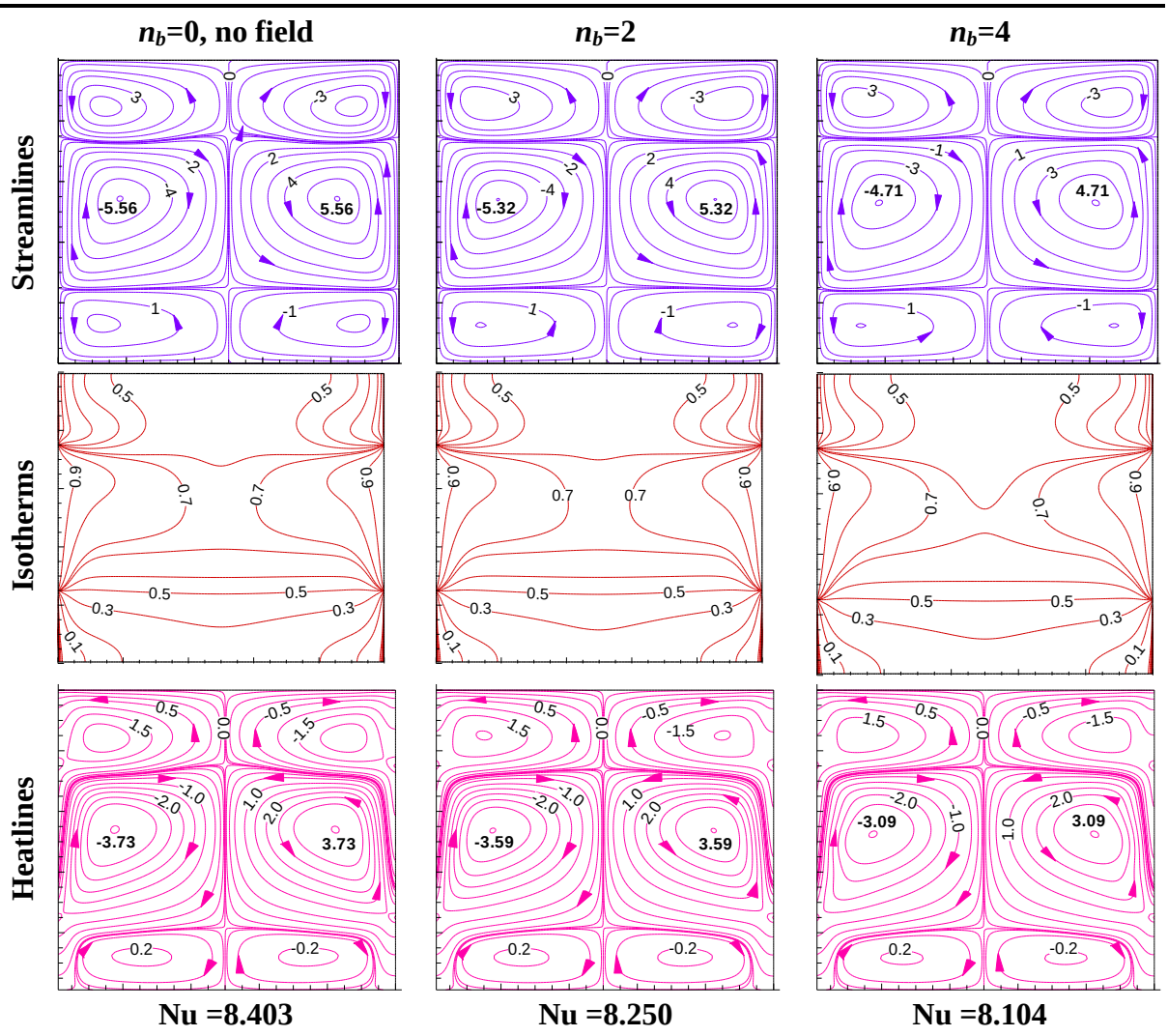

Fig. 32: Variation of thermo-fluid contours with MM heating in an un-tilted square cavity for different numbers of horizontal magnetic segments at Ha = 50, Da = 10^{-3}, Ra_m = 10^3, ϕ = 0.1%.

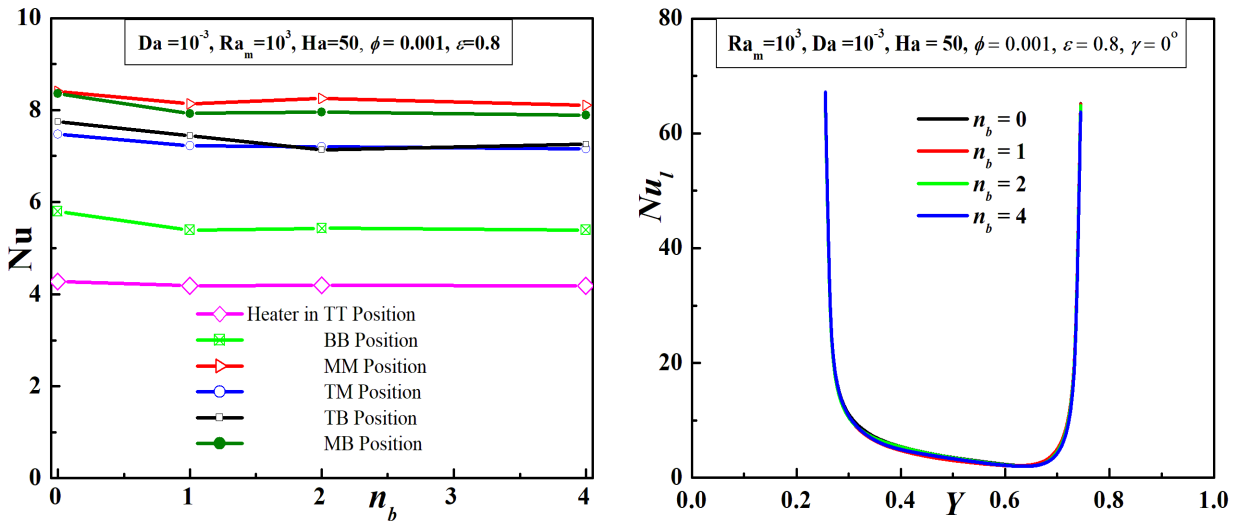

Fig. 33: Impact on heat transport in an un-tilted square cavity in terms of average Nu for different heating arrangements and local Nu with MM heating for different numbers of horizontal magnetic segments at Ha = 50, Da = 10^{-3}, Ra_m = 10^3, ϕ = 0.1%.

CHAPTER 4: CONCLUSIONS AND FUTURE SCOPE

Conclusions

In this study, the applications of segmental heating and magnetic fields in tilted cavities are explored. The research emphasizes the importance of heat transfer enhancement and investigates various parameters such as segmental heater lengths, magnetic field strengths, cavity angle, and the volume fraction of Cu-Al_2O_3 hybrid nanoparticles in the host fluid. The convective flow domain encompasses multiple physics including thermal buoyancy, nanofluid conductivity, flow-dampened porous medium, and magnetizing field.

The role of segmental heaters in controlling convective transport phenomena is examined for different values of modified-Rayleigh number, Darcy number, Rayleigh number, and Hartmann number. The study meticulously demonstrates the influence of cavity tilt, heater length, heater number, and other flow parameters. Numerical simulations are conducted to investigate the hydrothermal behavior of a hybrid nanofluid-filled tilted porous cavity heated in segments on both sidewalls. In addition, the effect of the segmented magnetizing field is explored by shifting the position of the partial magnetic fields (at the top, bottom, and middle) acting either horizontally or vertically. Furthermore, changing segment numbers (multi-segmenting), the magneto-hydrothermal behavior of the chosen thermal system is also analyzed and the thermal performance is evaluated by comparing the Nusselt numbers under two extremes, the absence of magnetic field and full-domain magnetizing field.

The study presents several conclusions based on the investigations:

- Segmented source walls lead to increased heat transportation rates compared to a single heated vertical wall, although the fluid circulation and energy circulation strength decrease. The heat transfer enhancement can reach up to approximately 245.79% compared to a single vertical wall as the heat source.
- The orientation of the cavity significantly affects the hydrothermal flow, especially when an active magnetizing field is applied. The highest heat transfer rate is observed in the vertical orientation, but tilting the cavity can increase heat transport by around 20.13% in the vertical position compared to no tilting.

- Symmetric or asymmetric combinations of fixed-length heaters have a significant impact on heat transfer. The combination of heaters at the TB position enhances heat transfer by up to approximately 185.33% compared to the TT position at a higher modified-Rayleigh number.
- Heat exchange enhancement is maximized at 48.29% for segmental heating with a variation of heater dimensions on either the left or right source walls.
- The use of multi-segmented heating sources demonstrates that increasing the number of heater segments leads to higher heat transfer rates. The heat transfer enhancement can reach a maximum of 285.98% (at a modified-Rayleigh number of 10^4) for ten (10) segmental heaters compared to two (2) heaters.
- Changing the aspect ratio (AR) of the cavity significantly alters the energy and fluid flow structure, affecting heat transfer. The maximum heat transfer enhancement is observed at an aspect ratio of 2, with an increase of up to 43% compared to an aspect ratio of 0.5.
- The circulation strength in cells varies with different values of modified-Rayleigh number, Darcy number, and porosity index. Heat transport increases with a higher modified-Rayleigh number and porosity but decreases with a higher Darcy number.
- The inclusion of nanoparticles in the fluid has a minor effect on the heat and fluid flow fields, but it results in an increase of approximately 3.20% in the average Nusselt number (Nu).
- The magnitude of the magnetizing force (Ha) influences the heat transport process. Increasing Ha reduces heat transfer, with a small decrease of approximately 18.40% compared to no magnetic field.
- The heat transportation rate varies with the angle of the horizontal magnetic field (β). The highest heat transfer is observed at β = 45°, and it decreases as the angle approaches β = 180°.
- Using a partially active magnetizing field allows for efficient control of flow fields. The reduction in heat transfer rate is lowest (around 13.97% to 10.88%) for the TB case compared to the entire domain magnetizing field.
- The presence of a mid-centered partial magnetizing field with fixed width influences the flow domain, creating vortices dependent on the segment length and the intensity of the magnetizing force. Heat transport is highest at the bottom location of the segment due to the high thermal buoyant force.

- Changing the direction of the partially active magnetizing fields can positively affect the transport phenomena. Both horizontal and vertical directions are explored, showcasing the control capabilities of altered magnetizing field directions.
- The study introduces the concept of multi-segmenting magnetizing fields as a more influential method for controlling convective transfer processes. The multi-segment system allows for adjustments in segment numbers, segmentwidths, and inter-segment gaps. Heat transfer reduction is maximized at approximately 7.01% with a fixed width of a multi-segmented magnetizing field ($n_b = 4$) compared to no segments ($n_b = 0$).

In conclusion, this study highlights the importance of segmental heaters and their positional and dimensional changes in enhancing heat transfer. The findings regarding multi-segmental heat sources, cavity inclination, and aspect ratio transformations provide valuable insights into heat transfer enhancement strategies. The influence of flow-dampening porous structures and magnetic fields is systematically presented. The study also explores the impact of field angle variation, change of segment width, segment position and direction shifting, and multi-banding. These findings contribute to the design of magneto-hydrothermal devices, offering potential alternatives for locally controlling heat transfer strategies.

Future Research Direction and Scope of Study

From the previous section, it is clear that this extensive work has been carried out on segmental heating, and application of full and partial magnetic fields, porous media filled with hybrid nanofluids. However, this study can be extended further. Future research directions and the scope of the study include the following:

- The extension of this work to wavy walled enclosures by modifying the square geometry to explore the effect of increased surface area on heat transfer.
- Utilizing machine learning techniques to predict the Nusselt number and friction factor of hybrid nanofluids in transition and turbulent flow regimes.
- Employing neural networks to predict the thermo-physical properties of various hybrid nanofluids, enabling more accurate modeling and characterization.
- Developing precise models that accurately characterize the fluid flow and heat transfer characteristics of hybrid nanofluids, enhancing our understanding of their behavior.
- Exploring the application of environmentally friendly nanofluids in everyday essential commodities, such as lubricants, solar water heating systems, and heat

exchange devices.

- Designing heat exchangers specifically tailored to harness the potential of hybrid nanofluids while addressing issues like heavy fouling.
- Conducting extensive investigations on the applications of hybrid nanofluids for free convection in rectangular and non-linear geometries, as well as non-circular channels.
- Anticipating the use of 3D modeling for practical applications of thermal management, considering a wide range of parametric influences as needed.

By exploring these future research directions, we can further enhance our understanding of segmental heating, magnetic fields, and the application of hybrid nanofluids, ultimately contributing to the development of more efficient and environmentally friendly thermal management systems and devices.

REFERENCES

Abu-Nada E, 2015, Dissipative particle dynamics simulation of combined convection in a vertical lid driven cavity with a corner heater.Int J Thermal Sci. 92, pp. 72–84.

Ahmed SE, Oztop HF, Salem KA, 2014, Natural convection coupled with radiation heat transfer in an inclined porous cavity with corner heater. Comp Fluids. 102, pp. 74–84.

Ali HF, 2020, Hybrid Nanofluids for Convection Heat Transfer. 1st ed, Academic Press, Elsevier.

Al-Rashed AAAA, Kolsi L, Oztop HF, Aydi A, Malekshah EH, Abu-Hamdeh N, Borjini MN, 2018, 3D magneto-convective heat transfer in CNT-nanofluid filled cavity under partially active magnetic field. Physica E 99, pp. 294–303.

Alsabery AI, Ismael MA, Chamkha AJ, Hashim I, 2019, Effects of two-phase nanofluid model on MHD mixed convection in a lid-driven cavity in the presence of conductive inner block and corner heater. J Thermal Anal Calorim 135, pp. 729–750.

Baghsaz S, Rezanejad S, Moghimi M, 2019, Numerical investigation of transient natural convection and entropy generation analysis in a porous cavity filled with nanofluid considering nanoparticles sedimentation. J. Mol. Liq. 279, pp. 327–341.

Begum AS, Nithyadevi N, Oztop HF, Al–Salem K, 2017, Numerical simulation of MHD mixed convection in a nanofluid filled non–Darcy porous enclosure. Int J Mech Sci.130, pp. 154–166.

Bejan A, Dincer I, Lorente S, Miguel AF, Reis AH, 2004, Porous and Complex Flow Structures in Modern Technologies.Springer, New York.

Biswas N, Mahapatra PS, Manna NK, 2016, Buoyancy-driven fluid and energy flow in protruded heater enclosure. Meccanica 5, pp. 2159–2184.

Biswas N, Manna NK, 2018, Magneto-hydrodynamic Marangoni flow in bottom-heated lid-driven cavity. J Mol Liq. 251, pp. 249–266.

Biswas N, Manna NK, Chamkha AJ, 2021, Effects of half-sinusoidal nonuniform heating during MHDthermal convection in Cu–Al2O3/water hybrid nanofluid saturated with porous media, J. Therm. Anal. Calorim. 143, pp. 1665–1688.

Brinkman HC, 1952, The viscosity of concentrated suspensions and solutions, J Chem Phys. 20, pp. 571-580.

Chamkha AJ, Rashad AM, Mansour MA, Armaghani T, Ghalambaz M, 2017, Effects of heat sink and source and entropy generation on MHD mixed convection of a Cu-water nanofluid in a lid-driven square porous enclosure with partial slip. Physics of Fluids 29, p. 052001-1–22.

Christiansen MG, Howe CM, Bono DC, Perreault DJ, Anikeeva P, 2017, Practical methods for generating alternating magnetic fields for biomedical research. Rev. Sci. Inst. 88, p. 084301.

Fritz S, Chaitow L, Hymel GM, 2008, Focused massage application, First edition: Clinical massage in healthcare setting, Mosby Elsevier Inc., Missouri, US pp. 314-379.

Ganguly R, Sen S and Puri IK, 2004, Thermomagnetic convection in a square enclosure using a line dipole. Phys. Fluids 16, pp. 2228–2236.

Geridonmez BP, Oztop HF, 2019, Natural convection in a cavity filled with porous medium under the effect of a partial magnetic field, Int. J. Mech. Sci. 161–162, p. 105077:1–10.

Geridonmez BP, Oztop HF 2020, Natural convection in a cavity under partial magnetic field applied from different corners, Int. Commun. Heat Mass Transfer 114, p. 104575.

Ghalambaz M, Mehryan SAM, Izadpanahi E, Chamkha AJ, Wen D, 2019, MHD natural convection of Cu–Al2O3 water hybrid nanofluids in a cavity equally divided into two parts by a vertical flexible partition membrane. J. Therm. Anal. Calorim. 138, pp. 1723–1743.

Ghalambaz M, Sabour M, Sazgara S, Pop I, Trâmbiţaş R, 2020, Insight into the dynamics of ferrohydrodynamic (FHD) and magnetohydrodynamic (MHD) nanofluids inside a hexagonal cavity in the presence of a non-uniform magnetic field. J. Magn. Magn.Mater. 497, p. 166024.

Ghasemi B, Aminossadati SM, Raisi A, 2011, Magnetic field effect on natural convection in a nanofluid-filled square enclosure. Int. J. Therm. Sci. 50, pp. 1748–1756.

Ghasemi K, Siavashi M, 2017, Lattice Boltzmann numerical simulation and entropy generation analysis of natural convection of nanofluid in a porous cavity with different linear temperature distributions on side walls. J. Mol. Liq. 233, pp. 415–430.

Gibanov NS, Sheremet MA, Oztop HF, Abu–Hamdeh N, 2017, Effect of uniform inclined magnetic field on mixed convection in a lid-driven cavity having a horizontal porous layer saturated with a ferrofluid. Int. J. Heat Mass Tranfer. 114, pp. 1086–1097.

Ismael MA, Abu–Nada E, Chamkha AJ, 2017, Mixed Convection in a square cavity filled with CuO–water nanofluid heated by corner heater. Int J Mech Sci. 133, pp. 42–50.

Jalil JM, Al-Tae'y KA, Ismail SJ, 2013, Natural convection in an enclosure with a partially active magnetic field, Numer. Heat Transfer A 64, pp. 72–91.

Huminic G, Huminic A, 2018, Hybrid nanofluids for heat transfer applications – A state-of the-art review. Int. J. Heat Mass Transfer 125, pp. 82–103.

Hussain S, Mehmood K, Sagheer M, 2016, MHD mixed convection and entropy generation of water–alumina nanofluid flow in a double lid driven cavity with discrete heating. J MagnMagn Mater. 419, pp. 140–155.

Javaherdeh K, Najjarnezami A, 2018, Lattice Boltzmann simulation of MHD natural convection in a cavity with porous media and sinusoidal temperature distribution. Appl. Math. Mech. Engl. Ed. 39, pp. 1187–1200.

Jmai R., Ben-Beya B, Lili T, 2016, Numerical analysis of mixed convection at various walls speed ratios in two-sided lid-driven cavity partially heated and filled with nanofluid, Journal of Molecular Liquids 221, pp. 691-713.

Kabeel AE, El-Said EMS, Dafea SA, 2015, A review of magnetic field effects on flow and heat transfer in liquids: present status and future potential for studies and applications. Renew. Sustain. Energy Rev. 45, pp. 830–837.

Kasaeian A, Daneshazarian R, Mahian O, Kolsi L, Chamkha AJ, Wongwises S, Pop I, 2017, Nanofluid flow and heat transfer in porous media: A review of the latest developments. International Journal of Heat and Mass Transfer 107, pp. 778–791.

Khaled AR, Vafai K, 2003, The role of porous media in modeling flow and heat transfer in biological tissues. Int. J. Heat Mass Transfer 46, pp. 4989–5003.

Khanafer K, Vafai K, 2019, Applications of nanofluids in porous medium. J. Thermal Anal. Calorim. 135, pp. 1479–1492.

Kumar A, Subudhi S, 2018, Preparation, characteristics, convection and applications of magnetic nanofluids: a review. Heat Mass Transfer 54, pp. 241–265.

Lin Y, Zhang B, Yan B, 2011, Enabling anticancer therapeutics by nanoparticle carriers: the delivery of paclitaxel. Int. J. Mol. Sci. 12, pp. 4395–4413.

Maghsoudi P., Siavashi M, 2019, Application of nanofluid and optimization of pore size arrangement of heterogeneous porous media to enhance mixed convection inside a two-sided lid-driven cavity. J Therm Anal Calorim. 135, pp. 947–961.

Malleswaran A, Sivasankaran S, 2016, A numerical simulation on MHD mixed convection in a lid–driven cavity with corner heaters. J ApplFl Mech. 9, pp. 311–319.

Manna, NK, Mondal C, Biswas N, Sarkar UK, Öztop HF, Abu-Hamdeh, NH, 2021a, Effect of multibanded magnetic field on convective heat transport in linearly heated porous systems filled with hybrid nanofluid, Physics of Fluids 33, p. 053604.

Manna NK, Mondal MK, Biswas N, 2021b, A novel multi-banding application of magnetic field to convective transport system filled with porous medium and hybrid nanofluid, PhysicaScripta 96, p. 065001.

Maxwell J, 1904, A treatise on electricity and magnetism, Vol 2, 3rd ed., Oxford University Press, Cambridge, UK.

Mehryan SAM, Izadi M, Chamkha AJ, Sheremet M, 2018, Natural convection and entropy generation of a ferrofluid in a square enclosure under the effect of a horizontal periodic magnetic field. J. Mol. Liq. 263, pp. 510–525.

M'hamed B., Sidik NAC, Yazid MNAWM, Mamat R, Najafi GKGHR, 2016, A review on why researchers apply external magnetic field on nanofluids. Int. Commun. Heat Mass Transfer 78, pp. 60–67.

Mondal MK, Biswas N, Mandal DK, Manna NK, Chamkha AJ, 2022, Assessment of thermal performance of hybrid nanofluid flow in a tilted porous enclosure by imposing partial magnetic fields, Waves in Random and Complex Media, DOI:10.1080/17455030.2022.2066220.

Muneeshwaran M, Srinivasan G, Muthukumar P, Wang C-C, 2021, Role of hybrid-nanofluid in heat transfer enhancement – a review. IntCommun Heat Mass Transfer 125, p. 105341.

Nasr KB, Chouikh R, Kerkeni C, Guizani A, 2006, Numerical study of the natural convection in cavity heated from the lower corner and cooled from the ceiling. Appl. Therm. Eng. 26, pp. 772–775.

Ozoe H, Okada K, 1989, The effect of the direction of the external magnetic field on the three-dimensional natural convection in a cubical enclosure. Int. J. Heat Mass Transfer 32, pp. 1939–1954.

Oztop HF, Salem KA, Pop I, 2011, MHD mixed convection in a lid–driven cavity with corner heater. Int J Heat Mass Tranfer. 54, pp. 3494–3504.

Puri IK, Ganguly R 2014 Particle transport in therapeutic magnetic fields Annu. Rev. Fluid Mech. 46, pp. 407–440.

Patankar SV, 1980, Numerical heat transfer and fluid flow. New York NY: Hemisphere.

Rashad AM, Mansour MA, Armaghani, T, Chamkha, AJ, 2019, MHD mixed convection and entropy generation of nanofluid in a lid-driven U-shaped cavity with internal heat and partial slip, Physics of Fluids 31, pp. 42006-1–17.

Rashidi S, Esfahani JA, Maskaniyan M, 2017 Applications of magnetohydrodynamics in biological systems–a review on the numerical studies. J MagnMagn Mater. 439, pp. 358–372.

Ray S, Chatterjee D., 2014, MHD mixed convection in a lid–driven cavity including heat conducting circular solid object and corner heaters with Joule heating. Int. Commun. Heat Mass Transfer 57, 200–207.

Selimefendigil F, Chamkha AJ, 2021, MHD mixed convection of Ag–MgO/water nanofluid in a triangular shape partitioned lid-driven square cavity involving a porous compound, Journal of Thermal Analysis and Calorimetry 143, pp. 1467-1484.

Selimefendigil F, ÖztopHakan F, Chamkha AJ, 2016, MHD mixed convection and entropy generation of nanofluid filled lid driven cavity under the influence of inclined magnetic fields imposed to its upper and lower diagonal triangular domains. J MagnMagn Mater 406, pp. 266–281.

Sheikholeslami M, 2017, Magnetohydrodynamicnanofluid forced convection in a porous lid driven cubic cavity using Lattice Boltzmann method. J Mol Liq. 231, pp. 555–565.

Sheikholeslami M, Chamkha AJ, 2016, Flow and convective heat transfer of a ferro-nanofluid in a double-sided lid-driven cavity with a wavy wall in the presence of a variable magnetic field. Numer Heat Transfer A. 69, pp. 1186-1200.

Sheikholeslami M, Rokni HB, 2017, Simulation of nanofluid heat transfer in presence of magnetic field: a review, International Journal of Heat and Mass Transfer 115, pp. 1203-1233.

Sheremet M.A, Oztop HF, Pop I, Salem KA, 2016, MHD free convection in a wavy open porous tall cavity filled with nanofluids under an effect of corner heater. Int. J. Heat Mass Tranfer. 103, pp. 955–964.

Song KW, Tagawa T, 2018, Thermomagnetic convection of oxygen in a square enclosure under nonuniform magnetic field. Int. J. Thermal Sci. 125, pp. 52–65.

Suresh S, Venkitaraj K, Selvakumar P, Chandrasekar M, 2012, Effect of Al_2O_3–Cu/water hybrid nanofluid in heat transfer, Exp Therm Fluid Sci. 38, pp. 54–60.

Szabo PSB, and Früh WG, 2018, The transition from natural convection to thermomagnetic convection of a magnetic fluid in a nonuniform magnetic field. J. Magn. Magn.Mater. 447, pp. 116–123.

Tiwari RK, Das MK, 2007, Heat transfer augmentation in a two-sided lid-driven differentially heated square cavity utilizing nanofluids, International Journal of Heat and Mass Transfer 50, pp. 2002-2018.

Varol Y, Oztop HF, Koca A, Ozgen F, 2009, Natural convection and fluid flow in inclined enclosure with a corner heater. Appl. Therm. Engg. 29, pp. 340–350.